Version of Record: https://www.sciencedirect.com/science/article/pii/S0927025623003816
Manuscript_00ff677da3625a5fd1eb770b8c28ce96

A Free-Energy-Based and Interfacially Consistent Phase-Field Model for Solid-State Sintering without Artificial Void Generation

Qingcheng Yang[1, 2,3*], Yongxin Gao[1], Arkadz Kirshtein[4], Qiang Zhen[2,5,6], Chun Liu[7]

[1] Shanghai Key Laboratory of Mechanics in Energy Engineering, School of Mechanics and Engineering Science, Shanghai Institute of Applied Mathematics and Mechanics, Shanghai University, Shanghai 200072, China

[2] Zhejiang Laboratory, Hangzhou 311100, China

[3] Shanghai Institute of Aircraft Mechanics and Control, Shanghai 200072, China

[4] Department of Mathematics, Tufts University, Medford, MA 02155, USA

[5] Nano-Science and Technology Research Center, Shanghai University 200072, China

[6] School of Materials Science and Engineering, Shanghai University 200072, China

[7] Department of Applied Mathematics, Illinois Institute of Technology, 60616 Chicago, IL, USA

[*] Corresponding author, Email: qyang@shu.edu.cn, Tel: 86-18262060994.

Abstract

In this work, a new free-energy-based and interfacially consistent phase-field model for solid-state sintering has been proposed. A phase-field model is considered interfacially consistent if it does not generate any spurious voids at the junctions of grain boundaries in fully dense powder compacts during sintering. A mathematical analysis of Model I, a well-known and widely employed free-energy-based phase-field model, found that it may produce a spurious driving force at the junctions of grain boundaries, which could impede the kinetic pathway of grain growth. The locally generated non-physical porosity is significantly affected by the ratio of specific grain boundary energy to specific surface energy. Building on Model I, a novel free-energy-based phase-field model, termed Model II, has been proposed to protect interfacial consistency by decoupling the respective surface energy and grain boundary energy contributions to the overall free energy of the system. The theoretical analysis of both models has been numerically confirmed. Finally, Model II has been validated by comparing the phase-field dihedral angles and dynamic neck growth with those obtained from analytical models and experiments. Given the freedom in formulating free energies as a function of phase-field variables, interfacial consistency could serve as a criterion for constructing phase-field models free from artificial phase generation.

Keywords: Phase-Field modeling; Interfacial consistency; Artificial void generation;
Microstructural evolution; Solid-state sintering

1. Introduction

As one of the most dominant materials processing techniques, sintering is the thermal consolidation of discrete powder ensembles to build a coherent compact component at elevated temperature (but below the melting point) [1-3]. As a major technological process with a long historical development, sintering has continually found new applications [4, 5]. For example, sintering is the crucial step in fabricating ceramic-based solid-state electrolytes for new batteries with better energy efficiency and safety [6, 7] and in the production of thermal interface materials in electronic devices with improved thermal performance [8, 9]. Other examples include the fabrication of ceramic and metal-based bioimplants from additive manufacturing [10], to name a few.

To develop new and improved materials with tailored microstructures and thus pre-defined properties, it is highly desirable to have a deep understanding of the sintering mechanisms and the accompanying microstructure evolution. Thermodynamically, the driving force for sintering is to reduce the surface energy of powder particle ensembles. Kinetically, surface energy reduction is achieved by the transport of materials to extend the contact area between particles and grains under appropriate conditions of temperature, pressure, and environment. In solid-state sintering, materials transport is generally achieved by cooperative surface diffusion, grain boundary diffusion, volume diffusion, rigid body motion, and vapor transport (evaporation-condensation) [11-14]. Due to the complex materials transport mechanisms, the dramatic and evolving geometry change, and the interplay with process parameters, it is challenging to predict the microstructure evolution during sintering with experiments[11, 15, 16] and analytical models [17-19] employing simplified geometries alone, calling for numerical modeling approaches[20].

Among the developed modeling schemes for solid-state sintering [21-46], the phase-field approach distinguishes itself from others by the appealing feature that the various materials diffusion mechanism involved in sintering can be naturally captured by introducing phase-field variables to define the corresponding diffusion path without explicitly tracking the evolving microstructure features, such as surfaces and grain boundaries [13, 47-70]. And the existing solid-state sintering models based on the phase-field approach may be classified into two

categories: the free-energy-based group [47] and the grand-potential-based group recently proposed in [55, 65, 71].

In the free-energy-based group, the energy of the discrete powder ensemble consists of surface energy and grain boundary energy. A conserved phase-field variable is employed to differentiate the powder grain phase and the surrounding vapor phase, and a set of non-conserved phase-field variables is used to differentiate powder grains with different crystal orientations. The key idea generally consists of two steps: (I) Thermodynamically, the free energy of the discrete powder ensemble is depicted as a function of the introduced phase-field variables; (II) Kinetically, the different material transport mechanisms and the accompanying microstructure changes are captured by the temporal and spatial evolutions of the introduced phase-filed variables governed by the respective Cahn-Hillard and Allen-Chan equations with the driving forces coming from reducing the defined free energy. One of the pioneering works in this group was originally proposed in [47] and is widely employed to study sintering under different conditions [48-54, 56-61, 66, 67].

In the recently proposed grand-potential-based category, instead of employing a free energy functional, the energy of the discrete powder ensemble consists of surface energy, grain boundary energy, and grand potential contributions from the respective solid and vapor phases. A non-conserved phase-field variable is employed to differentiate the powder phase and the surrounding vapor phase and a set of non-conserved phase-field variables is used to differentiate different grains. The mass conservation is achieved through the diffusion equation of phase concentrations and the Allen-Chan equations are employed to describe the evolution of the introduced phase-field variables. The key features of models in this group are that the interfacial properties are decoupled from the grand-chemical-potential contribution and that instead of solving for concentration, the evolution of the chemical potential is solved directly. Two representative models in this category have been proposed and they differ from each other through the employment of different formulations of the interfacial energies, with one using the obstacle-type potential energy term [55] and the other employing the multiwell-type energy contribution proposed in [65].

From the introduction of the respective category, it is seen that the two groups differ from each other in the following three aspects: (I) the free-energy-based approach does not introduce chemical energy contributions from the respective solid and vapor phases and considers only the interfacial energies; (II) the free-energy-based group employs a conserved order parameter to differentiate solid powder phase from the surrounding vapor phase while the grand-potential-based category uses a non-conserved phase-field variable; (III) the free-energy-based approach directly solves the Cahn-Hilliard equation for the conserved phase-field variable while the grand-potential-based group directly solve for the chemical potentials.

In this manuscript, we will focus on analyzing the free-energy-based approach. As a pioneering and representative example, the model proposed in [47] will be analyzed and is termed Model I in this work. Model I has been widely employed and extended to investigate the underlying physical mechanisms and microstructure evolutions under different processing conditions in sintering [48-54, 56-61, 66, 67]. For example, Model I was utilized to explore the condition under which grain growth is sensitive to the level of porosity [48]; the sintering of silver nanoparticles was investigated by Model I for applications as thermal interface materials [49]; the microstructure evolution in direct ink write (DIW) additive manufacturing was examined using Model I to explore the phase space of DIW process parameters with the target to find the ones that lead to optimal microstructures[60]. In addition, Model I has also been extended to incorporate the effects of non-isothermal conditions [51, 54, 61], elasticity[58], anisotropy of grain boundary[53], and external pressure[52] on the microstructure evolution under sintering.

However, there is a lack of mathematical and interfacial analysis of Model I. Specifically, the following key question has not been analyzed: is the phase-field free energy of the discrete powder particles under sintering interfacially consistent? Since free energy is the source to offer driving forces for microstructure evolution in sintering, it is highly worth analyzing. In this work, we provide a condition for interfacial consistency, which is stated as follows: phase-field free energy is termed interfacially consistent if it introduces no driving forces for an artificial void generation at the junctions of grain boundaries when the polycrystalline powder compact is fully consolidated. Physically, it means that if there is an absence of pores in the system, a void should

not be generated. It is worth noting that the interfacial consistency defined in this work is similar to the dynamical consistency mathematically defined in [72, 73].

In light of the absence of phase-field free energy analysis for sintering and upon the defined interfacial consistency, we perform a mathematical analysis of Model I and find that artificial voids may be generated locally at the junctions of grain boundaries in fully dense powder ensembles. Factors such as the ratio of specific grain boundary energy to specific surface energy significantly affect the amount of non-physical pore production in addition to their effect on pore and junction stabilities [74-76], which is also confirmed numerically. Furthermore, the relationship between materials properties and phase-field parameters in Model I may not be consistent in the sense that material grain boundary width is constrained to be equal to the surface thickness.

Motivated by these findings, we propose a novel phase-field model within the free-energy-based category, termed Model II in this work, to protect the defined interfacial consistency. The main idea is to decouple the respective surface energy and grain boundary energy contributions to the total phase-field free energy to ensure that the interfacial consistency in Model II is satisfied and that the map between materials properties and phase-field parameters is consistent without introducing constraints on the independent materials properties. Model II is also validated by comparing the results from both analytical models and experiments.

The rest of the manuscript is organized as follows. Section 2 first performs a theoretical analysis of the termed Model I to point out the source rooting for the interfacial inconsistency, and then proposes the named Mode II and shows its insurance of interfacial consistency. A comparison between grand-potential-based models and the free-energy-based Model II is also given in Section 2; Section 3 numerically confirms the theoretical findings analyzed in Section 2 by designing appropriate examples. Section 4 discusses the validity of the proposed Model II by comparing its dihedral angles and dynamic neck growth with that from analytical models and experiments. Section 5 concludes with closing remarks on the performance of the proposed phase-field model, and discusses the future research directions.

2. Theoretical analysis

This section introduces Model I which has been widely employed to describe the microstructure evolution in solid-state sintering. Then the interfacial consistency of Mode I is analyzed mathematically, where it is shown that artificial void generation may occur. Subsequently, a novel phase-field free energy of Model II is proposed and inspected to ensure interfacial consistency.

2.1 Model I

2.1.1 Model introduction

As mentioned in [47], both conserved and non-conserved phase fields are introduced to fully characterize the microstructure features involved in solid-state sintering, as shown in Fig. 1. The conserved phase-field C is introduced to differentiate the powder compact from the surrounding vapor phase and is defined as follows:

$$C = \frac{\rho}{\rho_0}, 0 \le \rho \le \rho_0 \tag{1}$$

where ρ is the density of the vapor-powder mixture, ρ_0 is the density of powder particles, and the density of the vapor phase is ignored. As such, C takes the value of 1 inside the powder compact, 0 in the vapor phase, and varies smoothly but sharply across the surface (vapor-particle interface). The non-conserved phase-field η_i is introduced to differentiate crystallographic orientations of powder particles and takes the value of 1 inside the ith particle, 0 elsewhere, and changes continuously but rapidly across the grain boundaries.

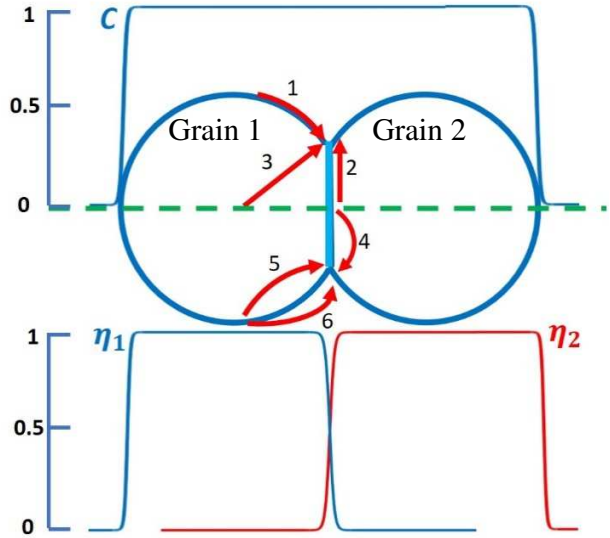

1. Surface Diffusion
2. Grain Boundary Diffusion
3. Volume Diffusion (Matter from Bulk)
4. Volume Diffusion (Matter from Bulk)
5. Volume Diffusion (Matter from Surface)
6. Evaporation-Condensation (Matter from Surface)

Fig. 1: Schematic illustration of different diffusion mechanisms and the profile of the introduced phase-fields C and η_i along the green line connecting the centers of the two grains.

After the introduction of phase-field variables to depict the microstructure features, the next step in phase-field formalism is to express the free energy $\mathcal{F}$ of the system of interest in terms of the defined phase fields. In general, the free energy $\mathcal{F}$ may be expressed as follows [47, 77]:

$$\mathcal{F} = \int_{\Omega} \left\{ f(C,\eta_i) + \frac{\kappa_C}{2}\|\nabla C\|^2 + \frac{\kappa_\eta}{2}\sum_{i=1}^{N_p}\|\nabla\eta_i\|^2 \right\} \mathrm{d}\Omega \tag{2}$$

and $f(C,\eta_i)$ is given as [47]:

$$f(C,\eta_i) = \alpha C^2(1-C)^2 + \beta\left[C^2 + 6(1-C)\sum_{i=1}^{N_p}\eta_i^2 - 4(2-C)\sum_{i=1}^{N_p}\eta_i^3 + 3\left(\sum_{i=1}^{N_p}\eta_i^2\right)^2\right] \tag{3}$$

Physically, $\mathcal{F}$ consists of surface and grain boundary energies. In Eq. (2), $f(C,\eta_i)$ is the bulk free energy density, α and β are model constants, κ_C and κ_η are the respective gradient coefficients for the conserved phase-field C and non-conserved phase-field η_i, and N_p is the total number of grains with different crystallographic orientations.

Then the driving forces for the evolution of the employed phase fields can be obtained through the variation of the free energy $\mathcal{F}$ to the corresponding phase field variable, i.e., $\frac{\delta\mathcal{F}}{\delta C}$ (Strictly speaking, $\frac{\delta\mathcal{F}}{\delta C}$ are the chemical potential of phase-field C and the gradient of $\frac{\delta\mathcal{F}}{\delta C}$ gives the driving

force) and $\frac{\delta \mathcal{F}}{\delta \eta_i}$, and their evolutions are governed through the modified Cahn-Hilliard and Allen-Cahn equations, respectively [47]:

$$\frac{\partial C}{\partial t} = \nabla \cdot \left(M \nabla \frac{\delta \mathcal{F}}{\delta C} \right) + \nabla \cdot \mathrm{J}_C + \xi_C \tag{4}$$

$$\frac{\partial \eta_i}{\partial t} = -L \frac{\delta \mathcal{F}}{\delta \eta_i} + \nabla \cdot \mathrm{J}_\eta + \xi_\eta \tag{5}$$

where M is the atomic mobility, L denotes the Allen-Cahn mobility, J_C and J_η are the respective flux contributions coming from rigid body motion, ξ_C and ξ_η are the Langevin noises. Theoretically, M is a second-order tensor. Since M is considered to be isotropic in this work, M is taken as a scalar. M describes the rate at which the measurable quantity defined by the phase-field C changes and may be related to the diffusion coefficient as follows to recover Fick's law [78]:

$$M = D^{eff} \left(\frac{\partial^2 \mathcal{F}}{\partial C^2} |_{C=1} \right)^{-1} \tag{6}$$

where D^{eff} is the effective diffusivity and is defined as:

$$D^{eff} = D^{vol} \phi(C) + D^{sf} C^2 (1 - C)^2 + 2 D^{gb} \sum_i^{N_p} \sum_{j \neq i}^{N_p} \eta_i \eta_j \tag{7}$$

where D^{sf}, D^{gb}, and D^{vol} are the respective surface, grain boundary, and volume diffusivities, $\phi(C)$ is an interpolation function given as $\phi(C) = C^3(10 - 15C + 6C^2)$. L describes the rate at which the structure of the atoms defined by the phase-field η changes with time, and may be estimated as [79]:

$$L = \frac{\vartheta_{gb} \gamma_{gb}}{\kappa_\eta} \tag{8}$$

where ϑ_{gb} is the grain boundary mobility and γ_{gb} is the specific grain boundary energy. As the phase fields C and η_i are introduced to depict microstructure features and the evolution of both phase fields through Eqs. (4) and (5) pictures the microstructure changes during solid-state sintering and guarantee that the microstructure is evolving in a direction that decreases the free energy $\mathcal{F}$ [80].

2.1.2 Analysis of the phase-field free energy

The phase-field free energy $\mathcal{F}$ in Section 2.1.1 has been widely employed in the community to predict microstructure evolution in solid-state sintering. This section analyses the interfacial consistency of $\mathcal{F}$: will artificial voids be generated at the junctions of grain boundaries in fully dense particle compacts?

Note that rigid body motion contributions (i.e. J_C and J_η) and Langevin noise terms (i.e. ξ_C and ξ_η) in Eqs. (4) and (5) are not considered when the following analysis is performed. This is based on the following reasons: (I) the driving force (i.e. $\frac{\delta\mathcal{F}}{\delta C}$) for artificial void generation (as will be shown in this section) comes solely from the proposed phase-field free energy $\mathcal{F}$, and is independent of the kinetic rigid body motion and Langevin noise, as seen in Eq. (4); (II) considering rigid-body motion and Langevin noise will make the voids purely generated from $\frac{\delta\mathcal{F}}{\delta C}$ less clear, as observed in Eq. (4); (III) for the numerical examples employed in this work, the kinetical mass transport path through rigid-body motion may be limited in already-dense particle compact (as will be shown in Section 3) and the focus here is on interfacial consistency, i.e., the phase-field free energy $\mathcal{F}$. As such, possible rigid-body motion is not considered in this work and will be employed in future extensions as suggested in [13, 14, 47].

According to Eq. (4), the driving force solely coming from the free energy $\mathcal{F}$ for the phase-field C is given as:

$$\frac{\delta\mathcal{F}}{\delta C} = 2\alpha C(1-C)(1-2C) + \beta\left(2C - 6\sum_{i=1}^{N_p}\eta_i^2 + 4\sum_{i=1}^{N_p}\eta_i^3\right) - \kappa_C\nabla^2 C \tag{9}$$

When the polycrystalline powder compact is fully consolidated and the vapor phase disappears, i.e., C =1 across the powder aggregates, we have:

$$\frac{\delta\mathcal{F}}{\delta C} = \beta S_\eta \tag{10}$$

where parameter β is a positive constant as will be given in section 2.1.3, and S_η is given as:

$$S_\eta = \left(2 - 6\sum_{i=1}^{N_p}\eta_i^2 + 4\sum_{i=1}^{N_p}\eta_i^3\right) \tag{11}$$

At the grain boundary between grains i and j, generally $S_\eta \neq 0$. For example, at the junction where three gains meet as shown in Fig. 2, supposing $\eta_1 = \eta_2 = \eta_2 = \frac{1}{3}$ (as $\sum_{i=1}^{3} \eta_i = 1$), we have $S_\eta = 0.44$, and when four grains meet, $S_\eta = 0.75$.

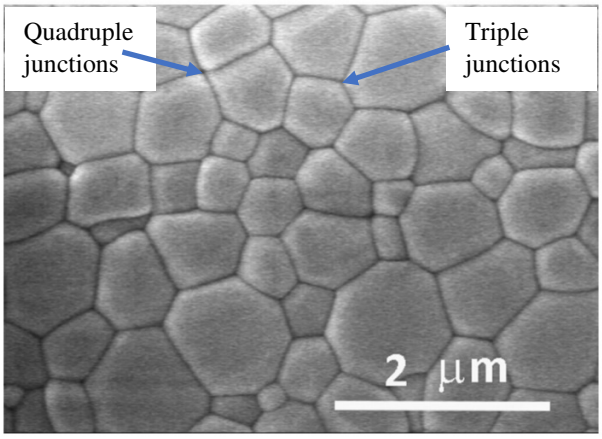

Fig. 2: Scanning electron microscope image of yttrium aluminum garnet after sintering for 3 min at 1400℃ [81].

Generally, since $\beta > 0$ and $S_\eta \neq 0$ at the junctions where grain boundaries meet, it is seen from Eq. (10) that the driving force for the phase-field C is not zero. As such, this spurious driving force may generate non-physical pores inside the fully solid powder compact. Note that: (I) if external pressure is applied to accelerate sintering (as is often employed in pressure-assisted sintering), the artificial voids will lead to local stress concentration and may serve as sources to initiate fictitious cracks; (II) if the predicted microstructure is employed to perform micromechanical analysis to obtain effective material properties of sintered products, the non-physical void generation will pollute the accuracy. Therefore, it may be important to ensure the interfacial consistency defined in this work.

When the phase-field model tends to generate voids, it creates more surfaces. Since the phase-field free energy $\mathcal{F}$ consists of surface energy and grain boundary energy, and the microstructure is evolving in a direction to reduce the total free energy, then the competition between specific grain boundary energy γ^{gb} and specific surface energy γ^{sf}, i.e., the ratio $\frac{\gamma^{gb}}{\gamma^{sf}}$, must have a significant effect on non-physical pore production. In Section 3.2, we will justify the aforementioned reasonings both mathematically and numerically.

2.1.3 Analysis of the phase-field parameters

Through a quantitative analysis procedure employed in [48, 79], the relationship between parameters α, β, κ_C and κ_η in the phase-field free energy $\mathcal{F}$ and material properties in Model I is derived and given as follows [48, 49, 79]:

$$\begin{cases} \gamma^{sf} = \frac{\sqrt{2}}{6}\sqrt{\kappa_C + \kappa_\eta}\sqrt{\alpha + 7\beta} \\ \gamma^{gb} = \frac{2}{\sqrt{3}}\sqrt{\beta\kappa_\eta} \\ \delta^{gb} = \sqrt{\frac{4\kappa_\eta}{3\beta}} \end{cases} \quad \text{or} \quad \begin{cases} \alpha = 12\frac{\gamma^{sf}}{\delta^{sf}} - 7\frac{\gamma^{gb}}{\delta^{gb}} \\ \beta = \frac{\gamma^{gb}}{\delta^{gb}} \\ \kappa_C = \frac{3}{2}\gamma^{sf}\delta^{sf} - \frac{3}{4}\gamma^{gb}\delta^{gb} \\ \kappa_\eta = \frac{3}{4}\gamma^{gb}\delta^{gb} \end{cases} \tag{12}$$

where δ^{gb} and δ^{sf} are the respective grain boundary width and surface thickness. Note that in Model I, the phase-field parameters α, β, κ_C and κ_η are constrained as follows[48, 49]:

$$\frac{6\beta}{\kappa_\eta} = \frac{\alpha+\beta}{\kappa_C} \tag{13}$$

As such, there are essentially 3 independent phase-field parameters. Since we have four material properties, i.e., γ^{gb}, γ^{sf}, δ^{gb}, and δ^{sf}, which, in general, are independent of each other, then there exists an inconsistency in the map between phase-field parameters and material properties, and there must be a hidden constraint on the material properties. Through a detailed analysis given in Appendix A, it is found that the constrain on the material properties is given as:

$$\delta^{sf} = \delta^{gb} \tag{14}$$

Since surface thickness δ^{sf} may be different from the grain boundary width δ^{gb} physically [34-36], Eq. (14) may introduce unnecessary constraints.

2.2 The proposed Model II

2.2.1 The novel phase-field free energy $\mathcal{F}^*$

Inspired by Model I and the analysis in Section 2.1, we propose a novel phase-field free energy $\mathcal{F}^*$ to assure interfacial consistency, and $\mathcal{F}^*$ is proposed as follows:

$$\mathcal{F}^* = \int_\Omega \left\{ f^*(C, \eta_i) + \frac{\kappa_C^*}{2}\|\nabla C\|^2 + \frac{\kappa_\eta^*}{2}N(C)\sum_{i=1}^{N_p}\|\nabla\eta_i\|^2 \right\} \mathrm{d}\Omega \tag{15}$$

and $f^*(C,\eta_i)$ is given as:

$$f^*(C,\eta_i) = \alpha^* C^2(1-C)^2 + \beta^* N(C)\left[1 - 4\sum_{i=1}^{N_p}\eta_i^3 + 3\left(\sum_{i=1}^{N_p}\eta_i^2\right)^2\right] \tag{16}$$

$$N(C) = C^2[1 + 2(1-C) + \epsilon(1-C)^2], \epsilon > 3 \tag{17}$$

where the starred symbols in Eqs. (15)-(17) are the counterparts of the quantities defined in Section 2.1, $N(C)$ is the employed interpolation function, and ϵ is a constant. To better discuss the structure and property of the proposed free energy $\mathcal{F}^*$, Eq. (15) is reorganized as follows:

$$\mathcal{F}^* = \mathcal{F}_{sf}^* + \mathcal{F}_{gb}^* \tag{18}$$

$$\mathcal{F}_{sf}^* = \int_\Omega \left(\alpha^* C^2(1-C)^2 + \frac{\kappa_C^*}{2}\|\nabla C\|^2\right) \mathrm{d}\Omega \tag{19}$$

$$\mathcal{F}_{gb}^* = \int_\Omega N(C)\left(\beta^*\left[1 - 4\sum_{i=1}^{N_p}\eta_i^3 + 3\left(\sum_{i=1}^{N_p}\eta_i^2\right)^2\right] + \frac{\kappa_\eta^*}{2}\sum_{i=1}^{N_p}\|\nabla\eta_i\|^2\right) \mathrm{d}\Omega \tag{20}$$

where $\mathcal{F}^*$ consists of surface energy $\mathcal{F}_{sf}^*$ and grain boundary energy $\mathcal{F}_{gb}^*$. The interpolation function $N(C)$ is carefully designed to decouple $\mathcal{F}_{sf}^*$ and $\mathcal{F}_{gb}^*$, and is plotted in Fig.3.

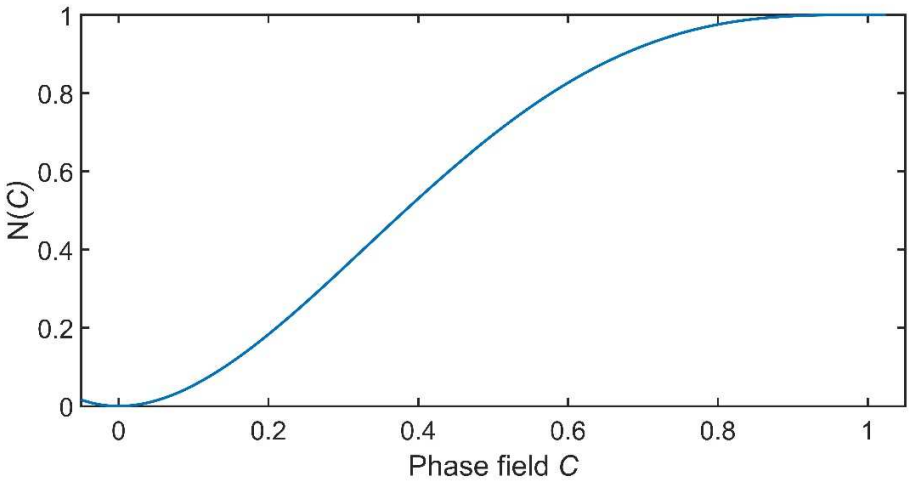

Fig. 3: The profile of the introduced interpolation function $N(C)$

As seen in Fig. 3, $N(C)|_{C=0} = 0$, $N(C)|_{C=1} = 1$.The parameter ϵ is required to be larger than 3 to ensure that $N(C)$ has a convex shape in the vicinity of C =1, and is taken to be 3.1 in this work. Then the equilibrium value of phase-field C is reached at $(C,\eta) = (1,1)$ or $(0,1)$, and the equilibrium value of non-conserved phase-field η_i is reached at $(C,\eta_i) = (1,1)$ with $\eta_{j\neq i} = 0$.

Note that in defining the novel free energy $\mathcal{F}^*$, the ith grain is represented by the product $C\eta_i$ as oppose to η_i in Model I.

As in [47], the evolution equations of introduced phase fields C and η_i are given as:

$$\frac{\partial C}{\partial t} = \nabla \cdot \left(M^* \nabla \frac{\delta \mathcal{F}^*}{\delta C} \right) \tag{21}$$

$$\frac{\partial \eta_i}{\partial t} = -L^* \frac{\delta \mathcal{F}^*}{\delta \eta_i} \tag{22}$$

with $M^* = D^{eff} \left(\frac{\partial^2 \mathcal{F}^*}{\partial C^2} |_{C=1} \right)^{-1}$ and $L^* = \frac{\vartheta_{gb} \gamma_{gb}}{\kappa_\eta^*}$. The proposed model is termed Model II in this work. Note that the rigid body motion and Langevin noises are not included in Model II in this work for the same reasons as discussed in Section 2.1.2.

2.2.2 Interfacial consistency analysis

The driving force coming from the phase-field free energy $\mathcal{F}^*$ in Model II for evolving the phase-field C is given as:

$$\frac{\delta \mathcal{F}^*}{\delta C} = g^*(C) + N'(C) \left(\beta^* S^*(\eta_i) + \frac{\kappa_\eta^*}{2} \sum_{i=1}^{N_p} \|\nabla \eta_i\|^2 \right) \tag{23}$$

where $g^*(C)$, $S^*(\eta_i)$, and $N'(C)$ are given as:

$$g^*(C) = 2\alpha^* C(1-C)(1-2C) - \kappa_C^* \nabla^2 C \tag{24}$$

$$S^*(\eta_i) = \left[1 - 4 \sum_{i=1}^{N_p} \eta_i^3 + 3 \left(\sum_{i=1}^{N_p} \eta_i^2 \right)^2 \right] \tag{25}$$

$$N'(C) = 2C(1-C)[3 + \epsilon(1-2C)] \tag{26}$$

To estimate the interfacial consistency of Model II, when the powder aggregates are fully solid, i.e., C=1 inside the powder phase, we have:

$$\frac{\delta \mathcal{F}^*}{\delta C} = 0 \tag{27}$$

Eq. (27) holds due to the property that $g^*(C)|_{C=1} = 0$ and $N'(C)|_{C=1} = 0$. As such, there is no artificial driving force for void generation in a fully dense region. Thus, Model II protects

interfacial consistency. In Section 3, we will numerically test the interfacial consistency of Model II.

2.2.3 The map between phase-field parameters and material properties

In this section, the relationship between the phase-field parameters α^*, β^*, κ_C^*, and κ_η^* in the proposed free energy $\mathcal{F}^*$ of Model II and material properties are derived through the quantitative analysis procedure in [48, 49, 79].

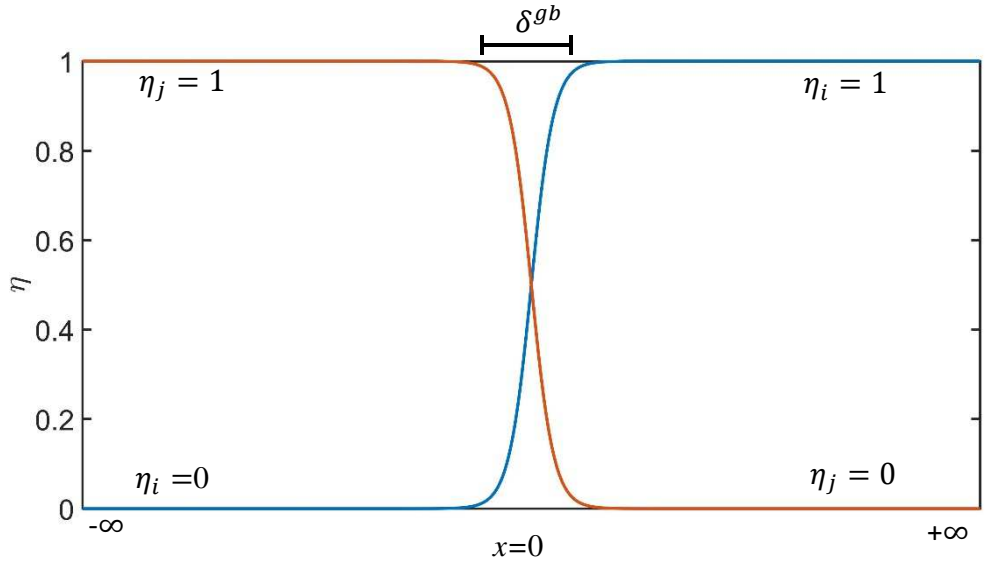

Fig. 4: The profile of the introduced phase-field η_i across a flat and diffuse grain boundary with a width δ^{gb}.

Assuming a flat grain boundary between two semi-infinite grains with the respective orientations i and j, the profile of η_i and η_j across the grain boundary along the x-direction perpendicular to the grain boundary may be shown as in Fig. 4 with a width of δ^{gb}. Then the specific grain boundary energy γ^{gb} may be defined as:

$$\gamma^{gb} = \int_{-\infty}^{+\infty} \left(f^*(C = 1, \eta_i, \eta_j) + \frac{\kappa_\eta^*}{2} \left\{ \left(\frac{\mathrm{d}\eta_i}{\mathrm{d}x} \right)^2 + \left(\frac{\mathrm{d}\eta_j}{\mathrm{d}x} \right)^2 \right\} \right) \mathrm{d}x \tag{28}$$

and f^* is given as:

$$f^*(C = 1, \eta_i, \eta_j) = \beta^* \left[1 - 4\left(\eta_i^3 + \eta_j^3\right) + 3\left(\eta_i^2 + \eta_j^2\right)^2 \right] \tag{29}$$

According to the Euler-Lagrangian equation, η_i and η_j satisfy the following equations as a stationary point of γ^{gb}:

$$\frac{\partial f^*(C=1,\eta_i,\eta_j)}{\partial \eta_i} - \kappa_\eta^* \frac{\mathrm{d}^2\eta_i}{\mathrm{d}x^2} = 0 \tag{30}$$

$$\frac{\partial f^*(C=1,\eta_i,\eta_j)}{\partial \eta_j} - \kappa_\eta^* \frac{\mathrm{d}^2\eta_j}{\mathrm{d}x^2} = 0 \tag{31}$$

For boundary conditions, we have:

$$\eta_i = 1 \text{ and } \eta_j = 0 \text{ for } x \longrightarrow +\infty \tag{32}$$

$$\eta_j = 1 \text{ and } \eta_i = 0 \text{ for } x \longrightarrow -\infty \tag{33}$$

$$\frac{\mathrm{d}\eta_i}{\mathrm{d}x} = \frac{\mathrm{d}\eta_j}{\mathrm{d}x} = 0 \text{ for } x \longrightarrow \pm\infty \tag{34}$$

Since Eq. (28) is symmetric to the profiles of η_i and η_j at $x = 0$, as shown in Fig. 4, we have:

$$\frac{\mathrm{d}\eta_j}{\mathrm{d}x} = -\frac{\mathrm{d}\eta_i}{\mathrm{d}x} \tag{35}$$

which gives: $\eta_i + \eta_j = const$. From the boundary condition given by Eq. (32), we have:

$$\eta_i + \eta_j = 1 \tag{36}$$

Based on Beltrami identity, we get:

$$f^*(C = 1, \eta_i, \eta_j) - \frac{\kappa_\eta^*}{2}\left[\left(\frac{\mathrm{d}\eta_i}{\mathrm{d}x}\right)^2 + \left(\frac{\mathrm{d}\eta_j}{\mathrm{d}x}\right)^2\right] = 0 \tag{37}$$

According to Eq. (35) and (37), the following holds:

$$\frac{\mathrm{d}\eta_i}{\mathrm{d}x} = \sqrt{\frac{f^*(C=1,\eta_i,\eta_j)}{\kappa_\eta^*}} \tag{38}$$

$$\frac{\mathrm{d}\eta_j}{\mathrm{d}x} = -\sqrt{\frac{f^*(C=1,\eta_i,\eta_j)}{\kappa_\eta^*}} \tag{39}$$

Substituting Eq. (37) into Eq. (28) gives,

$$\gamma^{gb} = \int_{-\infty}^{+\infty} 2f^*(C = 1, \eta_i, \eta_j)\mathrm{d}x \tag{40}$$

And the bulk free energy is obtained by substituting Eq. (36) into Eq. (29):

$$f^*\left(C=1,\eta_i,\eta_j=1-\eta_i\right)=12\beta^*\eta_i^2(1-\eta_i)^2 \tag{41}$$

Based on Eqs. (38) and (41), Eq. (40) can be rewritten as:

$$\gamma^{gb}=2\int_0^1 f^*\frac{\mathrm{d}x}{\mathrm{d}\eta_i}\mathrm{d}\eta_i=2\int_0^1 f^*\sqrt{\frac{\kappa_\eta^*}{f^*}}\mathrm{d}\eta_i=2\int_0^1\sqrt{12\beta^*\eta_i^2(1-\eta_i)^2\kappa_\eta^*}\mathrm{d}\eta_i=\frac{2}{\sqrt{3}}\sqrt{\beta^*\kappa_\eta^*} \tag{42}$$

As shown in Fig. 4, the grain boundary width δ^{gb} may be approximated as:

$$\frac{1}{\delta^{gb}}=\left(\frac{\mathrm{d}\eta_i}{\mathrm{d}x}\right)_{x=0}=\sqrt{\frac{f^*(\eta_i=0.5)}{\kappa_\eta^*}}=\sqrt{\frac{3\beta^*}{4\kappa_\eta^*}} \tag{43}$$

As such, the grain boundary thickness δ^{gb} may be estimated as:

$$\delta^{gb}=\sqrt{\frac{4\kappa_\eta^*}{3\beta^*}} \tag{44}$$

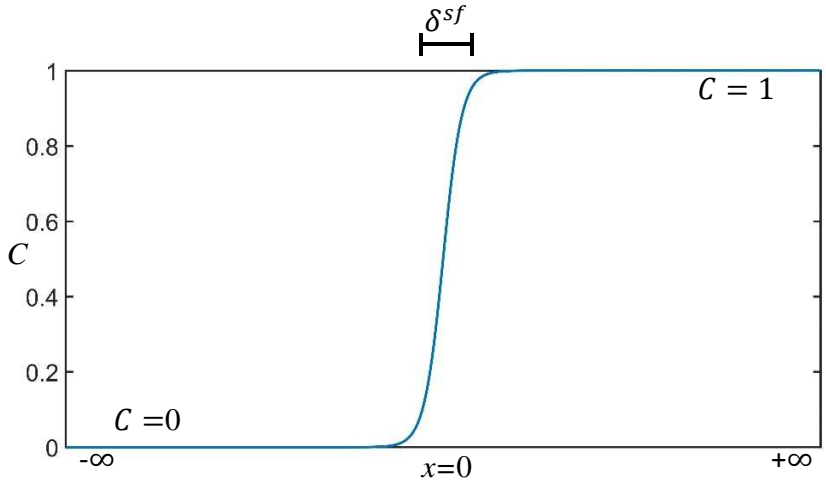

Fig. 5: A schematic of the introduced phase-field C across a flat and diffuse surface with a width δ^{sf}.

Next, we will derive the relationship between phase-field parameter α^*, κ_C^* and materials properties γ^{sf}, δ^{sf}. Assuming a flat surface between a semi-infinite solid grain and semi-infinite vapor phase, the profile of C along the x-direction perpendicular to the surface may be shown in

Fig. 5 with a surface thickness of δ^{sf}. The specific surface energy γ^{sf} may be evaluated as follows:

$$\gamma^{sf} = \int_{-\infty}^{+\infty} \left(f^*(C, \eta = 1) + \frac{\kappa_C^*}{2} \left(\frac{\mathrm{d}C}{\mathrm{d}x} \right)^2 \right) \mathrm{d}x \tag{45}$$

Note that in Eq. (45), $C\eta$ is employed to represent the grain phase in the proposed model to decouple the non-conserved phase-field η from estimating γ^{sf}. Then the bulk free energy density $f^*(C, \eta = 1)$ is given as:

$$f^*(C, \eta = 1) = \alpha^* C^2 (1 - C)^2 \tag{46}$$

Following the same procedure employed above, we have:

$$\frac{\partial f^*(C, \eta = 1)}{\partial C} - \kappa_C^* \left(\frac{\mathrm{d}^2 C}{\mathrm{d}x^2} \right) = 0 \tag{47}$$

$$f^*(C, \eta = 1) - \frac{\kappa_C^*}{2} \left(\frac{\mathrm{d}C}{\mathrm{d}x} \right)^2 = 0 \tag{48}$$

$$\frac{\mathrm{d}C}{\mathrm{d}x} = \sqrt{\frac{2 f^*(C, \eta = 1)}{\kappa_C^*}} \tag{49}$$

Substituting Eq. (48) into Eq. (45), we have:

$$\gamma^{sf} = \int_{-\infty}^{+\infty} 2 f^*(C, \eta = 1) \mathrm{d}x = \int_0^1 2 f^*(C, \eta = 1) \frac{\mathrm{d}x}{\mathrm{d}C} \mathrm{d}C = \frac{\sqrt{2 \kappa_C^* \alpha^*}}{6} \tag{50}$$

From the profile of $C(x)$ at equilibrium, the surface thickness may be estimated as:

$$\frac{1}{\delta^{sf}} = \left(\frac{\mathrm{d}C}{\mathrm{d}x} \right)_{x=0} = \sqrt{\frac{2 f^*(C = 0.5, \eta = 1)}{\kappa_C^*}} = \sqrt{\frac{\alpha^*}{8 \kappa_C^*}} \tag{51}$$

As such, the surface thickness δ^{sf} may be given as:

$$\delta^{sf} = \sqrt{\frac{8 \kappa_C^*}{\alpha^*}} \tag{52}$$

The map between the phase-field parameters α^*, β^*, κ_C^*, and $\kappa_\eta{}^*$ defined in Model II and material properties γ^{gb}, δ^{gb} γ^{sf}, δ^{sf} are summarized as follows:

$$\begin{cases} \gamma^{gb} = \frac{2}{\sqrt{3}}\sqrt{\beta^* \kappa_\eta^*} \\ \gamma^{sf} = \frac{\sqrt{2\kappa_C^* \alpha^*}}{6} \\ \delta^{gb} = \sqrt{\frac{4\kappa_\eta^*}{3\beta^*}} \\ \delta^{sf} = \sqrt{\frac{8\kappa_C^*}{\alpha^*}} \end{cases} \quad \text{or} \quad \begin{cases} \alpha^* = 12\frac{\gamma^{sf}}{\delta^{sf}} \\ \beta^* = \frac{\gamma^{gb}}{\delta^{gb}} \\ \kappa_C^* = \frac{3}{2}\gamma^{sf}\delta^{sf} \\ \kappa_\eta^* = \frac{3}{4}\gamma^{gb}\delta^{gb} \end{cases} \tag{53}$$

Since four independent model parameters α^*, β^*, κ_C^*, κ_η^* and four independent material properties γ^{gb}, γ^{sf}, δ^{gb}, and δ^{sf} are employed in Eq.(53), the map may fix the inconsistency between phase-field parameters and material properties in Mode I as introduced in Section 2.1 and does not constrain the relationship between δ^{sf} and δ^{gb}.

2.3 Comparison of grand-potential-based and free-energy-based sintering models

The grand-potential-based sintering models separate interfacial properties from extensive variables, such as the concentration field, which would otherwise contribute to the driving force for non-conserved phase-field variables. This separation is achieved by using the grand potential as a function of the intensive variable, i.e., the chemical potential, instead of using the free energy as a function of the concentration field [55, 65]. The proposed Model II uses a free-energy-based framework, but it still decouples the defined concentration, or conserved phase-field variable C, from grain boundary properties, as shown in Eq. (53).

As for artificial void generation, the grand-potential-based model in [65] does not introduce spurious voids thanks to the employment of the interpolation function proposed in [82] and the multiwell function proposed in [79, 82], which has been analyzed in [83]. Another grand-potential-based model in [55] employs third-order terms of non-conserved phase-field variables in the obstacle-type potential energy to suppress artificial phase generation at grain boundaries, which requires careful selection of the coefficient corresponding to the third-order term [84, 85]. The free-energy-based Model II proposed in this work also does not introduce artificial voids, as analyzed in Section 2.2.2.

As for model complexity, grand-potential-based models require more material parameters than free-energy-based Model II due to the introduction of grand potential contributions from the respective solid and vapor phases [55, 65]. In addition, since voids do not have measurable

energy, the parameters required to build up the grand potential may not be easily obtained. In contrast, the free-energy-based Model II proposed in this work does not involve grand potentials, so it only requires a considerably smaller subset of the material parameters needed in grand-potential-based models. Therefore, compared to grand-potential-based models, Model II is simpler to implement while sharing its advantages.

3. Numerical test

In this section, the interfacial consistency analyzed for both Model I and Model II in Section 2 is tested numerically. The factors that may affect the artificial void generation phenomenon are also investigated by numerical examples.

3.1 Numerical implementation

The Cahn-Hillard and Allen-Cahn equations in both Model I and Model II are solved by employing the central finite difference scheme in spatial discretization and a forward Euler method in the temporal domain. An intermediate variable μ^*, i.e., the chemical potential of phase-field C, is introduced to split the fourth-order Cahn-Hillard equation in Model II into two second-order equations as follows:

$$\frac{\partial C}{\partial t} = \nabla \cdot (M^* \nabla \mu^*) \tag{54}$$

$$\mu^* = \frac{\delta \mathcal{F}^*}{\delta C} = 2\alpha^* C(1-C)(1-2C) - \kappa_C^* \nabla^2 C + N'(C)\left(\beta^* S^*(\eta_i) + \frac{\kappa_\eta^*}{2}\sum_{i=1}^{N_p}\|\nabla \eta_i\|^2\right) \tag{55}$$

Then the central finite difference approach is employed to approximate the spatial derivatives in Eqs. (54) and (55). The same numerical scheme is also applied to Model I.

3.2 Artificial void generation

3.2.1 Triple junction case

Fig. 6a shows the microstructure consisting of three grains with grain boundaries represented by the yellow lines. Note that no vapor phase is surrounded initially to mode the locally dense regions of sintered product. The simulation domain is set to be $\Omega = (0,14\pi)^2$ and is spatially discretized by a 128×128 grid. The employed model parameters for Model I and Model II in this

setting are shown in Table 1. Since the map between phase-field parameters and materials properties in Model II is different from that in Model I, as shown in Eqs. (12) and (53), the employed phase-field parameters for Model II are also different from their counterparts employed in Model I to assure that both Model I and Model II have the same γ^{gb} and γ^{sf}.

Table 1 The normalized model parameters that were employed for Models I and II in the simulation. The diffusivities D and the mobility L were fixed to $D^{sf} = 960.0$, $D^{gb} = 96.0$, $D^{vol} = 9.6$ and $L = 1$, respectively.

Parameters / Model	$\alpha \parallel \alpha^*$	$\beta \parallel \beta^*$	$\kappa_C \parallel \kappa_C^*$	$\kappa_\eta \parallel \kappa_\eta^*$	γ^{gb}	γ^{sf}	γ^{gb}/γ^{sf}
Model I	16.00	16.00	4.05	12.00	16.00	10.67	1.50
Model II	128.00	16.00	16.00	12.00	16.00	10.67	1.50

In Fig. 6b and 6c, the microstructures are depicted through the phase-field C, represented by "CON" in the work unless otherwise mentioned, to better visualize if there is any void production. As such, grain boundaries are not shown in Figs. 6b and 6c. As defined in Section 2, C =1 represents the solid grain phase, C = 0 denotes the vapor phase, and any value in between represents a mixture of vapor and solid particle phases. Then the local porosity φ can be defined as: $\varphi = 1 - C$. Figures 6b and 6c select the respective transient microstructures from Models I and II when the largest local porosity φ_{max} is observed. The lower bound of the respective color bar is set to be 1-φ_{max} to better picture the produced void if any. As shown in Fig. 6b, Model I could open up a local porosity $\varphi = 9.4\%$ at the junction of grain boundaries, as observed from the color bar. In contrast, Model II introduces almost no local porosity. Since no vapor phase is present in the initial microstructure, the produced local porosity is non-physical. As such, the numerical results are consistent with the theoretical analysis in Section 2.

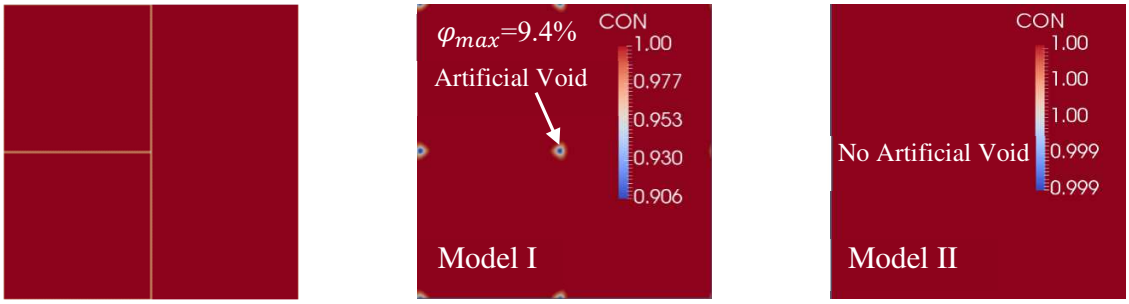

(a) (b) (c)

Fig. 6 : Microstructure morphologies from Model I and Model II: (a) initial grain structures for both Models I and II with solid yellow lines representing grain boundaries; (b) the selected microstructure corresponding to the transient local porosity $\varphi_{max} = 9.4\%$ observed from Model I; (c) the microstructure from Model II without producing local porosity. "CON" represents the phase-field *C*; To better visualize the produced voids, grain boundaries are not shown in (b) and (c). This coloring scheme is employed throughout this work unless otherwise mentioned.

3.2.2 Quadruple junction case

The quadruple junction is unstable and will split into two triple junctions [75, 76]. The purpose of employing a quadruple junction is to check if both models can capture the junction splitting process and the effects of non-physical voids on the kinetic splitting. The employed model parameters are shown in Table 2 for the quadruple junction case.

Table 2 The normalized model parameters that were employed for Models I and II in quadruple junction simulation. The diffusivities *D* and the mobility *L* were fixed to $D^{sf} = 960.0$, $D^{gb} = 96.0$, $D^{vol} = 9.6$ and $L = 1$, respectively.

Parameters / Model	$\alpha \parallel \alpha^*$	$\beta \parallel \beta^*$	$\kappa_C \parallel \kappa_C^*$	$\kappa_\eta \parallel \kappa_\eta^*$	γ^{gb}	γ^{sf}	γ^{gb}/γ^{sf}
Model I	16.00	10.59	3.32	7.94	10.59	7.51	1.41
Model II	90.12	10.59	11.27	7.94	10.59	7.51	1.41

Fig. 7a shows the initial quadruple junction of four equally sized grains for both Model I and Model II. From Figs. 7 and 8, it is observed that: (I) both Model I and Model II can capture the

quadruple-to-triple junction splitting instability, as shown in Figs. 8b and 8d; (II) Artificial voids have already been generated before the splitting process happens in Model I, as seen in Fig. 7b where a local porosity $\varphi_{max} = 20.09\%$ is produced; (III) Non-physical void generation may delay the microstructure evolution. Figs. 8b and 8d select the respective microstructures from Model I and Model II when the respective triple junctions reach the same spatial point $(6\pi, 6\pi)$, and it takes 15 seconds for Model I and 14.1 seconds for Model II to reach the selected location. This is due to that Model I initially decreases its free energy by producing artificial voids but without microstructure evolution, and has less energy left to drive grain boundary evolution thereafter; (IV) the non-physical and transient voids still exist after the splitting is finished in Model I, as shown in Fig. 8a; In contrast, almost no porosity is produced in Model II, as observed in Fig. 8c. Note that all the figures corresponding to the locally produced porosity in this work only select the microstructures when the transient porosity is observed and is not the final stable one.

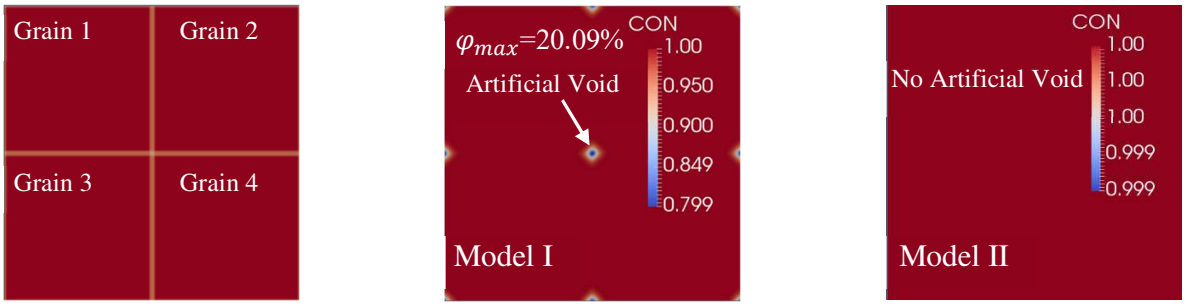

(a) (b) (c)

Fig. 7： Microstructure morphologies from Model I and Model II: (a) initial grain structures for both Models I and II with solid lines representing grain boundaries; (b) the selected microstructure corresponding to the transient local porosity$\varphi_{max} = 20.09\%$ observed before the splitting in Model I; (c) the microstructure from Model II without producing local porosity. "CON" represents the phase-field C throughout this work unless otherwise mentioned. To better visualize the produced voids, grain boundaries are not shown in (b) and (c).

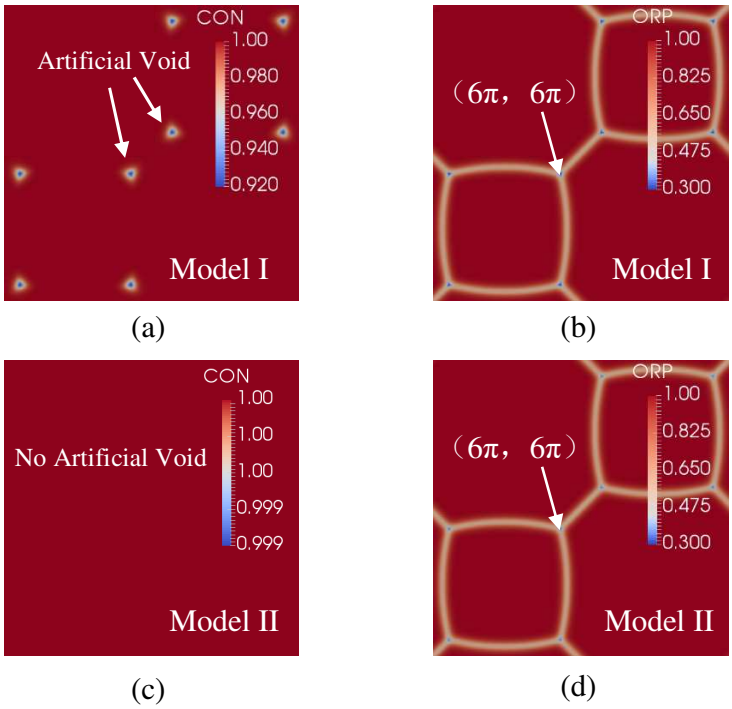

Fig. 8: Microstructure morphologies after the quadruple junction splitting into triple junctions from the respective Model I (a-b) when t = 15s and Model II (c-d) when t = 14.1s; the microstructure is pictured by respectively employing the phase-field C ("Con" in plots a and c) to view the particle compact as a whole and using the summation of $(C\eta_1)^2 + (C\eta_2)^2$ ("ORP" in plots b and d) to view individual grains.

3.3 Effect of rigid body motion

We note that the presence of non-physical pores may induce rigid body motion and potentially may lead to pore closure. To investigate the effect of rigid body motion on artificial pore generation, the advection term originally proposed in [47] is combined with Model I. The parameters employed in the advection term are also taken from [47] for the quadruple junction case. Figure 9 compares the cases with and without the inclusion of the advection term in Model I. Numerical results show that considering the advection term to account for rigid-body motion yields similar results as the one where the advection term is neglected. This observation may be attributed to the driving force behind artificial pore generation, which arises solely from the free energy and thus remains independent of kinetically mass transportation paths, as analyzed in

Section 2.1.2. Additionally, since pore generation primarily occurs within the junctions, it causes minimal rigid body motion within the dense grain systems.

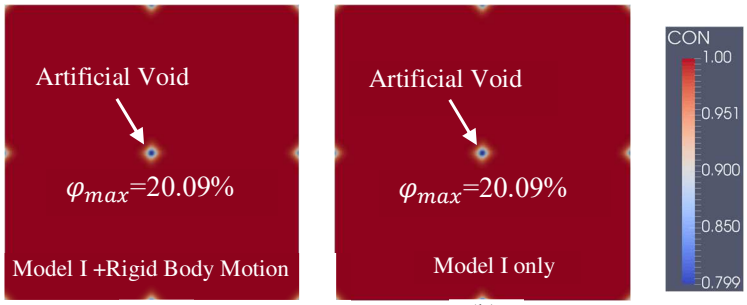

(a) (b)

Fig. 9: Artificial pore generation for Model I with (a) and without (b) rigid body motion, showcasing the transient local porosityφ_{max} of 20.09%.

3.4 Effect of the ratio $\frac{\gamma^{gb}}{\gamma^{sf}}$

Since the microstructure in sintering tends to evolve in a direction to decrease the total free energy $\mathcal{F}^*$ consisting of grain boundary energy$\mathcal{F}^*_{gb}$ and surface energy $\mathcal{F}^*_{sf}$, as shown in Eq. (18), and that the void production phenomenon creates surfaces by replacing grain boundaries, then the ratio $\frac{\gamma^{gb}}{\gamma^{sf}}$ may have significant effect on artificial pore generation. To numerically test how the ratio $\frac{\gamma^{gb}}{\gamma^{sf}}$ affects the void production in Model I, four different ratios of $\frac{\gamma^{gb}}{\gamma^{sf}}$ are employed, and the model parameters corresponding to each ratio are given in Table 3. Note that the phase-field parameters are adjusted to reach the specified ratio of $\frac{\gamma^{gb}}{\gamma^{sf}}$ according to their map with material properties as shown in Eq. (12).

Table 3 The normalized parameters employed in Model I. The diffusivities D and the mobility L were fixed to $D^{sf} = 960.0$, $D^{gb} = 96.0$, $D^{vol} = 9.6$ and $L = 1$, respectively.

Parameters / Cases	α	β	κ_C	κ_η	γ^{gb}	γ^{sf}	γ^{gb}/γ^{sf}	φ_{max}
I	16.00	1.00	2.13	0.75	1.00	1.92	0.52	1.44%
II	16.00	3.20	2.40	2.40	3.20	3.20	1.00	4.89%
III	16.00	10.59	3.32	7.94	10.59	7.51	1.41	20.09%
IV	16.00	16.00	4.05	12.00	16.00	10.67	1.50	86.00%

All the test cases have the same initial microstructure as shown in Fig. 7a. Figure 10 selects the microstructure morphologies when the local and largest transient porosities $\varphi_{max}$is reached for the respective setting of $\frac{\gamma^{gb}}{\gamma^{sf}}$. The difference (1- φ_{max}) is employed as the lower bound of the color bars for the respective ratios, and φ_{max} is listed in Table 3 for each case. It is seen that the ratio $\frac{\gamma^{gb}}{\gamma^{sf}}$ significantly influences the local porosity generated at the grain boundary junctions. The locally introduced φ_{max} increases as the ratio $\frac{\gamma^{gb}}{\gamma^{sf}}$ rises. Physically, this is due to the fact that generating more voids (thus more surfaces are replacing grain boundaries) at grain boundary junctions helps decrease the total free energy of the system as $\frac{\gamma^{gb}}{\gamma^{sf}}$ increases. Mathematically, according to Eqs. (12) and (13), the ratio $\frac{\gamma^{gb}}{\gamma^{sf}}$ in Model I can be expressed as:

$$\frac{\gamma^{gb}}{\gamma^{sf}} = \frac{12}{\frac{\alpha}{\beta}+7}, \alpha > 0, \beta > 0 \tag{56}$$

For a fixed parameter α, $\frac{\gamma^{gb}}{\gamma^{sf}}$ rises when parameter β increases, as is employed in Table 3. From Eq. (10), the driving force for artificial void generation also becomes larger when β goes up for a fixed initial microstructure (and thus fixed S_n in Eq. (10)). As such, the driving force for fictitious pore productions is proportional to the ratio $\frac{\gamma^{gb}}{\gamma^{sf}}$, and the transient porosity φ_{max} increases due to the locally enlarged driving force as the ratio $\frac{\gamma^{gb}}{\gamma^{sf}}$ increases. Note that Model II

produces similar microstructures as shown in Fig. 7c for all the employed ratios of $\frac{\gamma^{gb}}{\gamma^{sf}}$ in Table 3, and almost no local porosity is observed. As such, the microstructures from Model II are not shown for simplicity.

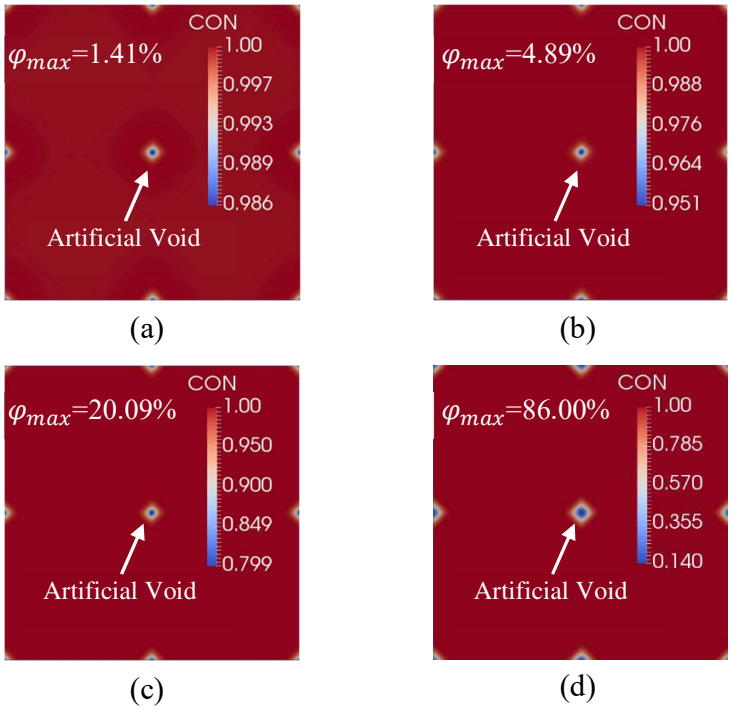

Fig. 10: Artificial void productions in Model I when the local and largest transient porosity φ_{max} is reached for different ratios of γ^{gb}/γ^{sf}: (a) $\gamma^{gb}/\gamma^{sf} = 0.52$, (b) $\gamma^{gb}/\gamma^{sf} = 1.00$, (c) $\gamma^{gb}/\gamma^{sf} = 1.41$, and (d) $\gamma^{gb}/\gamma^{sf} = 1.50$.

To better visualize the regions that could be affected by artificial void production, a threshold of $\varphi = 5\%$ is employed, i.e., the lower bound of the color bar is set to be 0.95. Figures 11a and 11b re-depict the voids corresponding to the transient porosity φ_{max} when $\gamma^{gb}/\gamma^{sf} = 1.41$ and $\gamma^{gb}/\gamma^{sf} = 1.50$, respectively. The domain with dark blue color represents the locations where at least a local porosity of $\varphi = 5\%$ has been produced.

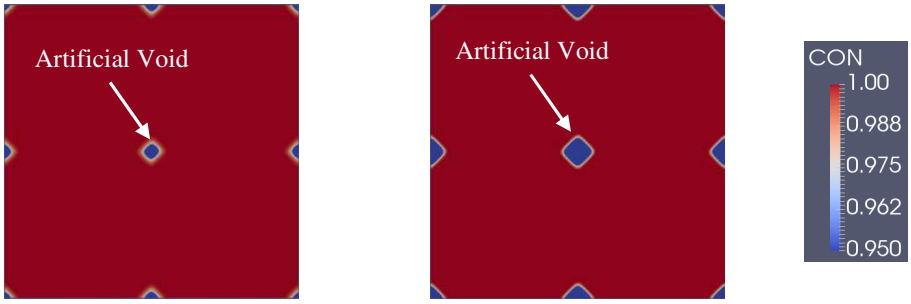

(a) (b)

Fig. 11: Microstructure morphologies with dark blue regions representing the locations where at least a local porosity of $\varphi = 5\%$ is produced: (a) $\gamma^{gb}/\gamma^{sf} = 1.41$, (b) $\gamma^{gb}/\gamma^{sf} = 1.50$.

3.5 Discussion

Note that the ratio $\frac{\gamma^{gb}}{\gamma^{sf}}$ is related to pore stability as analyzed in [74]. As shown in Fig. 10, the ratio $\frac{\gamma^{gb}}{\gamma^{sf}}$ also significantly affect the generation of the transient porosity φ_{max}. It is worth noting that their effect on φ_{max} is in addition to that on pore and junction stabilities in the sense that the transient porosity φ_{max} does not exist within the initial microstructure and is instead generated artificially due to the interfacial inconsistency defined in this work. When external stress is applied to assist sintering, as in pressure-assisted sintering, φ_{max} will introduce local stress concentrations and may offer spurious sites to initiate defects, such as cracks, and may change the kinetic evolution path. As such, even though φ_{max} may be transient, it may be necessary to remove the non-physical porosity φ_{max} if a more accurate kinetic process is wanted.

4. Validation and application of Model II

The interfacial consistency of the proposed Model II has been theoretically protected in Section 2 and has also been numerically confirmed in Section 3. In this section, Model II will be validated against both theoretical models and sintering experiments.

4.1 Dihedral angle

According to [1-3], the theoretical dihedral angle between two equally-sized particles at sintering equilibrium is given as:

$$\gamma^{gb} = 2\gamma^{sf}\cos\left(\frac{\theta}{2}\right) \tag{57}$$

where θ is the dihedral angle shown in Fig. 12. By adjusting the ratio $\frac{\gamma^{gb}}{\gamma^{sf}}$, different dihedral angles can be reached. In this study, the ratio is set to be 1.0 and 1.5, respectively, with θ to be 120° and 83° accordingly. The corresponding phase-field simulations are performed with the parameter settings in Table 4. The dihedral angles predicted from the respective phase-field analysis are shown in Fig. 12, where a good agreement with Eq. (57) is achieved.

Table 4 . The employed phase-field parameters for the proposed Model II in the dihedral angle study with $D^{sf} = 2304.0$, $D^{gb} = 230.4$, $D^{vol} = 23.04$, $L = 1$ for $\frac{\gamma^{gb}}{\gamma^{sf}} = 1.00$ and $D^{sf} = 7680.0$, $D^{gb} = 768.0$, $D^{vol} = 76.8$, $L = 1$ for $\frac{\gamma^{gb}}{\gamma^{sf}} = 1.50$.

α^*	β^*	κ_C^*	κ_η^*	γ^{gb}	γ^{sf}	γ^{gb}/γ^{sf}
38.40	3.20	4.80	2.40	3.20	3.20	1.00
128.00	16.00	16.00	12.00	16.00	10.67	1.50

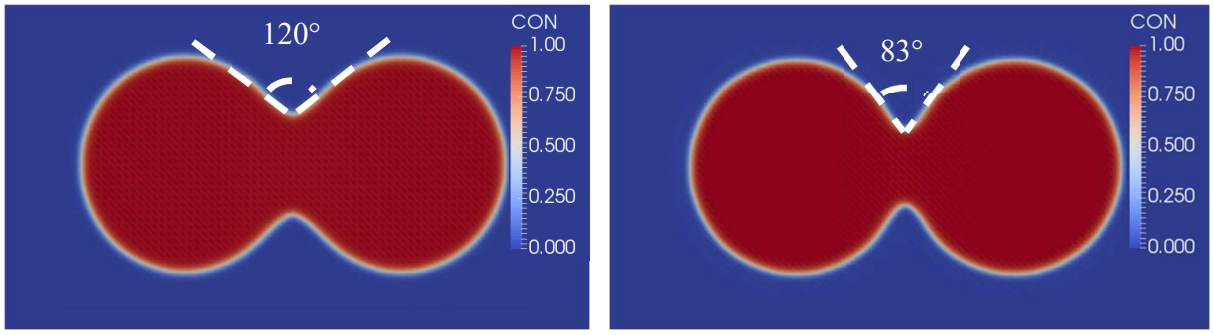

(a) (b)

Fig. 12: the phase-field dihedral angles from Model II with (a) $\gamma^{gb}/\gamma^{sf} = 1.0$, θ =120°, and (b) $\gamma^{gb}/\gamma^{sf} = 1.5$, θ =83°.

4.2 Neck growth

In this section, the same two-particle model as employed in Section 4.1 is also used to check the validity of Model II by comparing the dynamic neck growth as a function of time from both phase-field simulation and theoretical analysis.

The theoretical neck growth of the employed two-particle model may follow a power-law form given by [19]:

$$\left(\frac{X}{D_p}\right)^n = Bt \tag{58}$$

where X is the neck length, D_p is the particle diameter, t is time, and B is a constant related to geometrical assumptions and material properties. Note that the exponent n in Eq. (58) may be different for different diffusion mechanisms, and may also differ among different theoretical models employing different assumptions of geometrical simplifications [19]. For example, n could take the value of 5, 6, or 7 for surface diffusion under different analytical models.

In the phase-field simulation, the neck diameter X is normally evaluated as $X = \int \frac{\eta_i \eta_j}{\delta^{gb}} dA$ [49]. However, for the proposed Model II, it is found that the following evaluation of X matches the actually neck diameter observed numerically, as mentioned in [57]:

$$X = 6 \int \left\{ \frac{(C\eta_i)(C\eta_j)}{\delta^{gb}} \right\} dA \tag{59}$$

The validity of Eq. (59) is given in Appendix B.

Table 5 Comparison of the phase-field exponents n with theoretical counterparts under different diffusion mechanisms

Diffusion mechanism	n (t < 10)	n (t < 20)	n ($t < 100$)	n (theoretical)
I: All diffusion mechanisms	6.25	6.47	6.64	6,7
II: Grain boundary diffusion	5.97	7.48	8.70	6
III: Surface diffusion	4.06	4.57	5.40	5,6,7
IV: Volume diffusion	3.42	4.30	5.58	4,5

Thanks to the versatility of phase-field formalism, four different settings with the respective diffusion mechanisms in Table 5 are considered to check the capability of the proposed Model II to capture different diffusion mechanisms against theoretical models. Since analytical models are generally applicable when $\frac{X}{D_p} < 0.3$ [19], the data of the phase-field neck length X is fitted against Eq. (58) for $t < 10$, $t < 20$, and $t < 100$, respectively. The fitted exponent n for the respective phase-field setting and the theoretical values are given in Table 5, and the fitted power-law with all diffusion mechanisms activated is shown in Fig. 13. In general, the phase-field exponent n is within the theoretical range, and the discrepancy may be attributed to the fact that the geometry corresponding to the neck growth data employed in the phase-field fitting may differ from the ones simplified in the analytical models and that the fitted exponent n is sensitive to the data employed in the fitting process at different sintering stages (corresponding to different geometries of the two-particle model).

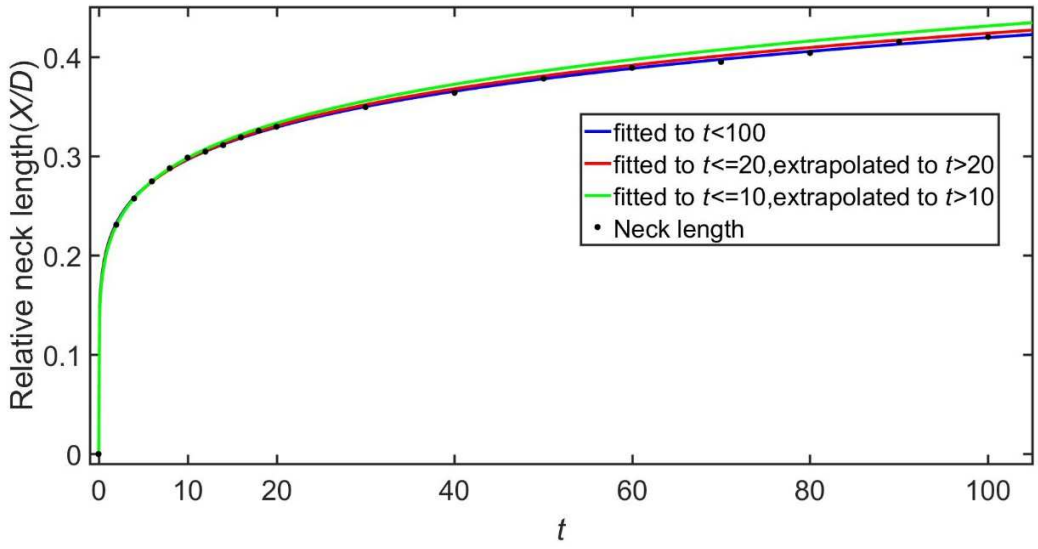

Fig. 13: Relative neck growth as a function of time t; scattered points are from phase-field simulation and solid lines are the fitted power-law corresponding to data employed in the fitting at different times.

4.3 Sintering experiment of silver nanoparticles

In this section, the proposed Model II is applied to the sintering process of silver nanoparticles and is compared to the experiment in [86]. The material parameters involved in the developed

phase-field framework are the grain boundary diffusion coefficient D^{gb}, surface diffusion coefficient D^{sf}, volume diffusion coefficient D^{vol}, grain boundary mobility ϑ^{gb}, specific grain boundary energy γ^{gb}, and specific surface energy γ^{sf}. The diffusion coefficient generally follows the Arrhenius equation given as:

$$D = D_0 e^{-\frac{Q}{k_b T}} \tag{60}$$

where D_0 is a temperature-independent constant, Q is the activation energy, T is the temperature, and k_b is the Boltzmann constant. The employed material properties are listed in Table 6. The grain boundary diffusivity D^{gb} is typically of the order between surface and volume diffusion coefficients, and is assigned to be $D^{gb} = 0.1D^{sf}$, as suggested in [47, 49].

Table 6 The employed material parameters of silver nanoparticles

Property	Value	Units	Reference
γ^{sf}	1.14	J m^{-2}	[87]
γ^{gb}	0.79	J m^{-2}	[88]
Q^{sf}	4.0 ×10^{-19}	J	[89]
D_0^{sf}	50	m^{2}s^{-1}	[89]
Q^{vol}	3.215 ×10^{-19}	J	[90]
D_0^{vol}	0.67 ×10^{-4}	m^{2}s^{-1}	[90]
ϑ^{gb}	10^{-16}	m^4 J^{-1} s^{-1}	[91]

According to the map between materials properties and phase-field parameters defined in Eq. (53), the values of the following model parameters are determined: $\alpha^* = 6.84\times10^9$ J/m^3, $\beta^* = 3.95\times10^8$ J/m^3, $\kappa_C^* = 3.42\times10^{-9}$ J/m, $\kappa_\eta^* = 1.185\times10^{-9}$ J/m. Note that since the surface thickness δ^{sf} is not available, δ^{sf} is assumed to be equal to the grain boundary width δ^{gb}, and is set a value of 2 nm. Then the employed phase-field parameters and diffusion coefficients are normalized to make them numerically friendly. The normalized parameters and materials properties are given in Table 7.

Table 7 Normalized phase-field parameters and material properties employed in the simulation of sintering of silver nanoparticles.

α^*	β^*	κ_C^*	κ_η^*	D^{sf}	D^{gb}	D^{vol}	L
17.32	1.00	19.48	6.75	22.88	2.29	0.14	26.33

The simulation domain is set to be 128 nm × 64 nm and is spatially discretized by a 192×96 grid. Figure 14 shows the microstructure evolution of two equally sized silver nanoparticles with a diameter of 40 nm sintered at 400 ℃ at different times, and is compared with experimental observations in [86]. A reasonable match is achieved between phase-field predictions and experimental inspections in terms of microstructure morphologies. As reported in [86], the presence of carbon on the particle surfaces introduces impurities and may change the surface diffusion coefficient. As such, the uncertainties in the employed material properties and the geometry difference between the phase-field powders and the actual particle shapes may account for the observed discrepancy.

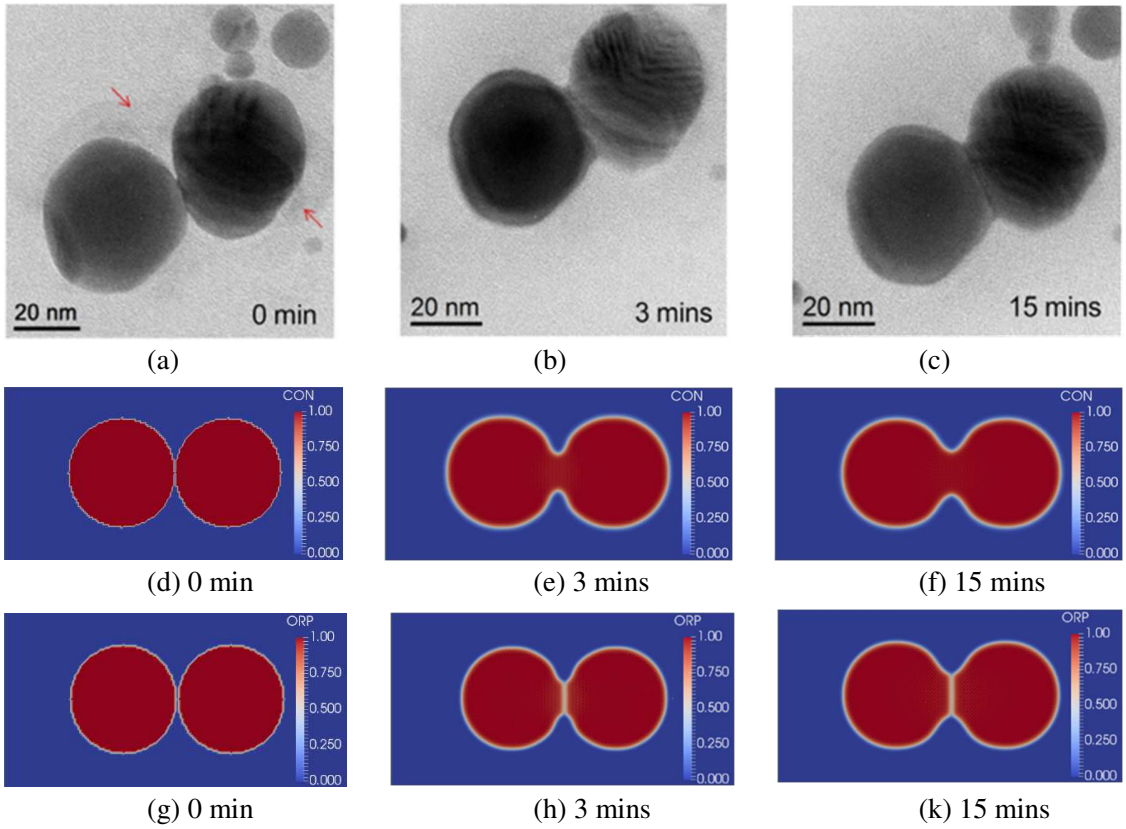

(a) (b) (c)

(d) 0 min (e) 3 mins (f) 15 mins

(g) 0 min (h) 3 mins (k) 15 mins

Fig. 14: Microstructure evolution of silver nanoparticles sintered at 400 ℃: (a-c) in situ TEM observations, and phase-field predictions. The microstructure is pictured by respectively employing the phase-field C ("Con" in plots d-f,) to view the particle compact as a whole, and using the summation of $(C\eta_1)^2 + (C\eta_2)^2$ ("ORP" in the plots g-f) to view individual grains.

5. Summary and Conclusions

This work is aimed to propose a novel free-energy-based and interfacially consistent phase-field model for solid-state sintering. In this work, the interfacial consistency is defined as follows: a phase-field model is termed interfacially consistent if the phase-field free energy does not offer a driving force for generating artificial voids at junctions of grain boundaries when the polycrystalline powder compact is fully dense. Physically, interfacial consistency means that a void should not be generated if it does not exist.

Through a mathematical analysis of the well-known and widely employed phase-field model in [47], which is termed Mode I in this work, it is found that artificial voids may be produced at the junctions of grain boundaries and that the ratio of specific grain boundary energy to specific surface energy $\frac{\gamma^{gb}}{\gamma^{sf}}$ has a significant effect on this non-physical pore generation, which is in addition to their effect on pore and junction stabilities as analyzed in [74-76]. Numerical tests have been performed to confirm the mathematical analysis. In addition, the phase-field model parameters in Model I may constrain the relationship between grain boundary width and surface thickness, which may introduce an inconsistent map between model parameters and material properties.

Inspired by Model I, a novel phase-field free energy, termed Model II in this work, is proposed and analyzed mathematically. By carefully decoupling the surface energy and grain boundary energy contributions to the total free energy, it is shown that the proposed free-energy-based phase-field model protects interfacial consistency analytically, which is also confirmed numerically under different settings. The phase-field parameters in Model II also free the constraint on grain boundary width and surface thickness and have a consistent map with material properties. In addition, Model II shares the advantages of the state-of-the-art phase-field models of sintering, the recent grand-potential-based models, while requiring a considerably smaller subset of the material parameters and being easier to implement.

The validity of Model II is tested by comparing the phase-field dihedral angles and dynamic neck growth with that from theoretical models and experiments. It is shown that the phase-field dihedral angles match well with the ones from theoretical predictions. The neck growth behavior from phase-field simulations has a reasonable agreement with that of the analytical models. The discrepancy may be due to the mismatch between the geometrical simplifications employed in theoretical analysis and the phase-field microstructure shape utilized for comparison. The microstructure evolution of silver nanoparticles from phase-field simulation also shows acceptable accuracy compared to the counterparts from sintering experiments. And the impurity-introduced uncertainty in the employed material parameters may account for the distinctions.

In the future, the incorporation of the rigid-body motion effect, especially in pressure-assisted sintering where external stress is applied to assist and accelerate sintering, will be pursued. The extension to non-isothermal sintering and the inclusion of grain boundary anisotropy are directions also worth pursuing.

Data Availability

Data will be made available on request.

Acknowledgments

Q.Y., Y.G, and Q.Z. acknowledge the financial support from the Key Research Project of Zhejiang Laboratory (No. 2021PE0AC02), the grant (No. 23010500400) from the Science and Technology Commission of Shanghai Municipality, and the key program (No. 52232002) from the Natural Science Foundation of China. C. L. is partially supported by NSF grants DMS-1950868 and DMS-2118181.

Appendix A

For a flat surface between a semi-infinite solid grain and a semi-infinite vapor phase, the specific surface energy γ^{sf} of Model I may be defined as follows:

$$\gamma^{sf} = \int_{-\infty}^{+\infty} \left(f(C,\eta) + \frac{\kappa_C}{2}\left(\frac{\mathrm{d}C}{\mathrm{d}x}\right)^2 + \frac{\kappa_\eta}{2}\left(\frac{\mathrm{d}\eta}{\mathrm{d}x}\right)^2 \right) dx \tag{A.1}$$

$$f(C,\eta) = \alpha C^2(1-C)^2 + \beta[C^2 + 6(1-C)\eta^2 - 4(2-C)\eta^3 + \eta^4] \tag{A.2}$$

with the *x*-direction perpendicular to the surface. According to the Euler-Lagrangian equation, C and η satisfy the following equations as a stationary point of γ^{sf}:

$$\frac{\partial f(C,\eta)}{\partial C} - \kappa_C\left(\frac{\mathrm{d}^2 C}{\mathrm{d}x^2}\right) = 0 \tag{A.3}$$

$$\frac{\partial f(C,\eta)}{\partial \eta} - \kappa_\eta\left(\frac{\mathrm{d}^2 \eta}{\mathrm{d}x^2}\right) = 0 \tag{A.4}$$

with boundary conditions given as:

$$C = 1 \text{ and } \eta = 1 \text{ for } x \longrightarrow +\infty \tag{A.5}$$

$$C = 0 \text{ and } \eta = 0 \text{ for } x \longrightarrow -\infty \tag{A.6}$$

Across the surface (vapor-particle interface), it may be reasonable to expect that：

$$\frac{\mathrm{d}\eta}{\mathrm{d}x} \propto \frac{\mathrm{d}C}{\mathrm{d}x} \tag{A.7}$$

And when boundary conditions are applied, we have:

$$C(x) = \eta(x) \tag{A.8}$$

$$\frac{\mathrm{d}\eta}{\mathrm{d}x} = \frac{\mathrm{d}C}{\mathrm{d}x} \tag{A.9}$$

Based on Beltrami identity, the following holds:

$$f(C,\eta) - \left[\frac{\kappa_\eta}{2}\left(\frac{\mathrm{d}\eta}{\mathrm{d}x}\right)^2 + \frac{\kappa_C}{2}\left(\frac{\mathrm{d}C}{\mathrm{d}x}\right)^2\right] = 0 \tag{A.10}$$

Substituting Eq. (A.9) to Eq. (A.10) and Eq. (A.8) into Eq. (A.2), we have:

$$\frac{\mathrm{d}C}{\mathrm{d}x} = \frac{\mathrm{d}\eta}{\mathrm{d}x} = \sqrt{\frac{2}{\kappa_C+\kappa_\eta} f(C,\eta)} \tag{A.11}$$

$$f(C,\eta = C) = (\alpha + 7\beta)C^2(1-C)^2 \tag{A.12}$$

The surface thickness δ^{sf} may be estimated as follows:

$$\frac{1}{\delta^{sf}} = \left(\frac{dC}{dx}\right)_{x=0} = \sqrt{\frac{2}{\kappa_C+\kappa_\eta} f(C,\eta)_{C=\eta=0.5}} = \sqrt{\frac{\alpha+7\beta}{8(\kappa_C+\kappa_\eta)}} \tag{A.13}$$

Then δ^{sf} is given as:

$$\delta^{sf} = \sqrt{\frac{8(\kappa_c+\kappa_\eta)}{\alpha+7\beta}} \tag{A.14}$$

As in Eq. (13), parameters α, β , κ_c and κ_η are constrained as $\frac{6\beta}{\kappa_\eta} = \frac{\alpha+\beta}{\kappa_C}$, which gives:

$$\frac{6\beta}{\kappa_\eta} = \frac{\alpha+7\beta}{\kappa_C+\kappa_\eta} \tag{A.15}$$

Plugging Eq. (A.15) into Eq. (A.14), we have:

$$\delta^{sf} = \sqrt{\frac{4\kappa_\eta}{3\beta}} \tag{A.16}$$

From Eq. (12), $\delta^{gb} = \sqrt{\frac{4\kappa_\eta}{3\beta}}$. Thus, we get:

$$\delta^{sf} = \delta^{gb} \tag{A.17}$$

Appendix B

In 2D, according to the equality of the grain boundary area, the following equation may hold:

$$\omega\left(\int_{-\frac{\lambda}{2}}^{\frac{\lambda}{2}}\int_{-\frac{\delta_{gb}}{2}}^{\frac{\delta_{gb}}{2}} \eta_i\eta_j dx\, dy\right) = \delta_{gb}\lambda, -\frac{\delta_{gb}}{2} \le x \le \frac{\delta_{gb}}{2}, -\frac{\lambda}{2} \le y \le \frac{\lambda}{2} \tag{B.1}$$

where ω is a constant, δ_{gb} is the grain boundary width, and λ is the neck length. Assuming a linear profile of η_i across the grain boundary, as employed in the evaluation of grain boundary width, we may have:

$$\eta_i = \frac{1}{\delta_{gb}}x + \frac{1}{2}, -\frac{\delta_{gb}}{2} \le x \le \frac{\delta_{gb}}{2} \tag{B.2}$$

$$\eta_j = -\frac{1}{\delta_{gb}}x + \frac{1}{2}, -\frac{\delta_{gb}}{2} \le x \le \frac{\delta_{gb}}{2} \tag{B.3}$$

Substituting Eqs. (B.2) and (B.3) into Eq. (B.1), we get:

$$\omega\left(\int_{-\frac{\delta_{gb}}{2}}^{\frac{\delta_{gb}}{2}}\left(-\frac{1}{\delta_{gb}}x + \frac{1}{2}\right)\left(\frac{1}{\delta_{gb}}x + \frac{1}{2}\right)dx\right) = \delta_{gb} \tag{B.4}$$

$$\omega\left(\frac{1}{4}x - \frac{1}{{\delta_{gb}}^2}x^3\right)\Big|_{-\frac{\delta_{gb}}{2}}^{\frac{\delta_{gb}}{2}} = \delta_{gb} \tag{B.5}$$

From Eq. (B.5), we have:

$$\frac{1}{6}\omega\delta_{gb} = \delta_{gb} \tag{B.6}$$

As such, the constant $\omega = 6$ and the neck length λ is evaluated as:

$$\lambda = \omega\int\frac{\eta_i\eta_j}{\delta_{gb}}dA \tag{B.7}$$

Since the *i*th grain in the proposed Model II is represented by $C\eta_i$, the neck length is calculated as:

$$\lambda = 6\int\left\{\frac{(C\eta_i)(C\eta_j)}{\delta^{gb}}\right\}dA \tag{B.8}$$

References

[1] M.N. Rahaman, Sintering of ceramics, CRC press, 2007.
[2] S.-J.L. Kang, Sintering: densification, grain growth and microstructure, Elsevier, 2004.
[3] R. German, Sintering: from empirical observations to scientific principles, Butterworth-Heinemann, 2014.
[4] R.K. Bordia, S.J.L. Kang, E.A. Olevsky, Current understanding and future research directions at the onset of the next century of sintering science and technology, Journal of the American Ceramic Society, 100 (2017) 2314-2352.
[5] N. Tuncer, A. Bose, Solid-state metal additive manufacturing: a review, Jom, 72 (2020) 3090-3111.

[6] S. Ramakumar, C. Deviannapoorani, L. Dhivya, L.S. Shankar, R. Murugan, Lithium garnets: Synthesis, structure, Li+ conductivity, Li+ dynamics and applications, Progress in Materials Science, 88 (2017) 325-411.
[7] M. Wood, X. Gao, R. Shi, T.W. Heo, J.A. Espitia, E.B. Duoss, B.C. Wood, J. Ye, Exploring the relationship between solvent-assisted ball milling, particle size, and sintering temperature in garnet-type solid electrolytes, Journal of Power Sources, 484 (2021) 229252.
[8] T. Wang, X. Chen, G.-Q. Lu, G.-Y. Lei, Low-temperature sintering with nano-silver paste in die-attached interconnection, journal of electronic materials, 36 (2007) 1333-1340.
[9] S.A. Paknejad, S.H. Mannan, Review of silver nanoparticle based die attach materials for high power/temperature applications, Microelectronics Reliability, 70 (2017) 1-11.
[10] B. Song, C. Kenel, D.C. Dunand, 3D ink-extrusion printing and sintering of Ti, Ti-TiB and Ti-TiC microlattices, Additive Manufacturing, 35 (2020) 101412.
[11] R. Grupp, M. Nöthe, B. Kieback, J. Banhart, Cooperative material transport during the early stage of sintering, Nature Communications, 2 (2011) 1-6.
[12] F. Wakai, G. Okuma, Rigid body motion of multiple particles in solid-state sintering, Acta Materialia, (2022) 118092.
[13] R. Shi, M. Wood, T.W. Heo, B.C. Wood, J. Ye, Towards understanding particle rigid-body motion during solid-state sintering, Journal of the European Ceramic Society, 41 (2021) 211-231.
[14] M. Seiz, Effect of rigid body motion in phase-field models of solid-state sintering, Computational Materials Science, 215 (2022) 111756.
[15] G.N. Bouala, N. Clavier, J. Léchelle, J. Monnier, C. Ricolleau, N. Dacheux, R. Podor, High-temperature electron microscopy study of ThO2 microspheres sintering, Journal of the European Ceramic Society, 37 (2017) 727-738.
[16] G. Okuma, N. Saito, K. Mizuno, Y. Iwazaki, H. Kishi, A. Takeuchi, M. Uesugi, K. Uesugi, F. Wakai, Microstructural evolution of electrodes in sintering of multi-layer ceramic capacitors (MLCC) observed by synchrotron X-ray nano-CT, Acta Materialia, 206 (2021) 116605.
[17] F. Wakai, O. Guillon, G. Okuma, N. Nishiyama, Sintering forces acting among particles during sintering by grain-boundary/surface diffusion, Journal of the American Ceramic Society, 102 (2019) 538-547.
[18] F. Wakai, K. Brakke, Mechanics of sintering for coupled grain boundary and surface diffusion, Acta materialia, 59 (2011) 5379-5387.
[19] W. Coblenz, J. Dynys, R. Cannon, R. Coble, Initial stage solid state sintering models. A critical analysis and assessment, Sintering Processes. Materials Science Research, 13 (1980) 141-157.
[20] E.A. Olevsky, V. Tikare, T. Garino, Multi-scale study of sintering: a review, Journal of the American Ceramic Society, 89 (2006) 1914-1922.
[21] A.G. Jinka, R.W. Lewis, Finite element simulation of hot isostatic pressing of metal powders, Computer methods in applied mechanics and engineering, 114 (1994) 249-272.
[22] J.M. Harmon, K. Karapiperis, L. Li, S. Moreland, J.E. Andrade, Modeling connected granular media: Particle bonding within the level set discrete element method, Computer Methods in Applied Mechanics and Engineering, 373 (2021) 113486.
[23] J.C. Steuben, A.P. Iliopoulos, J.G. Michopoulos, Discrete element modeling of particle-based additive manufacturing processes, Computer Methods in Applied Mechanics and Engineering, 305 (2016) 537-561.

[24] K. Mori, Finite element simulation of powder forming and sintering, Computer methods in applied mechanics and engineering, 195 (2006) 6737-6749.
[25] S. Chen, Y. Xu, Y. Jiao, Modeling morphology evolution and densification during solid-state sintering via kinetic Monte Carlo simulation, Modelling and Simulation in Materials Science and Engineering, 24 (2016) 085003.
[26] C. Martin, L. Schneider, L. Olmos, D. Bouvard, Discrete element modeling of metallic powder sintering, Scripta materialia, 55 (2006) 425-428.
[27] L. Ding, R.L. Davidchack, J. Pan, A molecular dynamics study of sintering between nanoparticles, Computational Materials Science, 45 (2009) 247-256.
[28] H. Zhu, R. Averback, Molecular dynamics simulations of densification processes in nanocrystalline materials, Materials Science and Engineering: A, 204 (1995) 96-100.
[29] S. Kucherenko, J. Pan, J. Yeomans, A combined finite element and finite difference scheme for computer simulation of microstructure evolution and its application to pore–boundary separation during sintering, Computational materials science, 18 (2000) 76-92.
[30] R. Bjørk, H.L. Frandsen, V. Tikare, E. Olevsky, N. Pryds, Strain in the mesoscale kinetic Monte Carlo model for sintering, Computational materials science, 82 (2014) 293-297.
[31] V. Tikare, M. Braginsky, D. Bouvard, A. Vagnon, Numerical simulation of microstructural evolution during sintering at the mesoscale in a 3D powder compact, Computational Materials Science, 48 (2010) 317-325.
[32] S. Nosewicz, J. Rojek, K. Pietrzak, M. Chmielewski, Viscoelastic discrete element model of powder sintering, Powder Technology, 246 (2013) 157-168.
[33] A. Jagota, P. Dawson, Micromechanical modeling of powder compacts—II. Truss formulation of discrete packings, Acta Metallurgica, 36 (1988) 2563-2573.
[34] V. Ivannikov, F. Thomsen, T. Ebel, R. Willumeit–Römer, Coupling the discrete element method and solid state diffusion equations for modeling of metallic powders sintering, Computational Particle Mechanics, (2022) 1-23.
[35] F. Thomsen, T. Ebel, R. Willumeit-Roemer, Simulation of neck growth and shrinkage for realistic temperature profiles–Determination of diffusion coefficients in a practical oriented procedure, Scripta Materialia, 168 (2019) 108-113.
[36] F. Thomsen, G. Hofmann, T. Ebel, R. Willumeit-Römer, An elementary simulation model for neck growth and shrinkage during solid phase sintering, Materialia, 3 (2018) 338-346.
[37] D. Wang, Y. Bai, C. Xue, Q. Wang, H. Yu, Z. Yan, Grain evolution simulation of ceramic tool material in spark plasma sintering process based on an improved cellular automata model, Ceramics International, 47 (2021) 13669-13677.
[38] M. Fattahi, M.N. Ershadi, M. Vajdi, F.S. Moghanlou, A.S. Namini, M.S. Asl, On the simulation of spark plasma sintered TiB2 ultra high temperature ceramics: a numerical approach, Ceramics International, 46 (2020) 14787-14795.
[39] M. Reiterer, T. Kraft, U. Janosovits, H. Riedel, Finite element simulation of cold isostatic pressing and sintering of SiC components, Ceramics International, 30 (2004) 177-183.
[40] H. Ch'ng, J. Pan, Cubic spline elements for modelling microstructural evolution of materials controlled by solid-state diffusion and grain-boundary migration, Journal of Computational Physics, 196 (2004) 724-750.
[41] H. Ch'ng, J. Pan, Modelling microstructural evolution of porous polycrystalline materials and a numerical study of anisotropic sintering, Journal of computational physics, 204 (2005) 430-461.

[42] W.J. Menz, R.I. Patterson, W. Wagner, M. Kraft, Application of stochastic weighted algorithms to a multidimensional silica particle model, Journal of Computational Physics, 248 (2013) 221-234.
[43] C.S. Lindberg, M.Y. Manuputty, E.K. Yapp, J. Akroyd, R. Xu, M. Kraft, A detailed particle model for polydisperse aggregate particles, Journal of Computational Physics, 397 (2019) 108799.
[44] D. Kempen, A. Piccolroaz, D. Bigoni, Thermomechanical modelling of ceramic pressing and subsequent sintering, International Journal of Mechanical Sciences, 156 (2019) 146-158.
[45] H. Xin, W. Sun, J. Fish, Discrete element simulations of powder-bed sintering-based additive manufacturing, International Journal of Mechanical Sciences, 149 (2018) 373-392.
[46] K. Mori, H. Matsubara, N. Noguchi, Micro–macro simulation of sintering process by coupling Monte Carlo and finite element methods, International journal of mechanical sciences, 46 (2004) 841-854.
[47] Y.U. Wang, Computer modeling and simulation of solid-state sintering: A phase field approach, Acta materialia, 54 (2006) 953-961.
[48] K. Ahmed, C. Yablinsky, A. Schulte, T. Allen, A. El-Azab, Phase field modeling of the effect of porosity on grain growth kinetics in polycrystalline ceramics, Modelling and Simulation in Materials Science and Engineering, 21 (2013) 065005.
[49] K. Chockalingam, V. Kouznetsova, O. Van der Sluis, M. Geers, 2D Phase field modeling of sintering of silver nanoparticles, Computer Methods in Applied Mechanics and Engineering, 312 (2016) 492-508.
[50] V. Ivannikov, F. Thomsen, T. Ebel, R. Willumeit-Römer, Capturing shrinkage and neck growth with phase field simulations of the solid state sintering, Modelling and Simulation in Materials Science and Engineering, 29 (2021) 075008.
[51] X. Wang, Y. Liu, L. Li, C.O. Yenusah, Y. Xiao, L. Chen, Multi-scale phase-field modeling of layer-by-layer powder compact densification during solid-state direct metal laser sintering, Materials & Design, 203 (2021) 109615.
[52] B. Dzepina, D. Balint, D. Dini, A phase field model of pressure-assisted sintering, Journal of the European Ceramic Society, 39 (2019) 173-182.
[53] S. Biswas, D. Schwen, H. Wang, M. Okuniewski, V. Tomar, Phase field modeling of sintering: Role of grain orientation and anisotropic properties, Computational materials science, 148 (2018) 307-319.
[54] X. Zhang, Y. Liao, A phase-field model for solid-state selective laser sintering of metallic materials, Powder technology, 339 (2018) 677-685.
[55] J. Hötzer, M. Seiz, M. Kellner, W. Rheinheimer, B. Nestler, Phase-field simulation of solid state sintering, Acta Materialia, 164 (2019) 184-195.
[56] Z. Zhang, X. Yao, P. Ge, Phase-field-model-based analysis of the effects of powder particle on porosities and densities in selective laser sintering additive manufacturing, International Journal of Mechanical Sciences, 166 (2020) 105230.
[57] W. Yan, W. Ma, Y. Shen, Powder sintering mechanisms during the pre-heating procedure of electron beam additive manufacturing, Materials Today Communications, 25 (2020) 101579.
[58] S. Biswas, D. Schwen, J. Singh, V. Tomar, A study of the evolution of microstructure and consolidation kinetics during sintering using a phase field modeling based approach, Extreme Mechanics Letters, 7 (2016) 78-89.
[59] R. Termuhlen, X. Chatzistavrou, J.D. Nicholas, H.-C. Yu, Three-dimensional phase field sintering simulations accounting for the rigid-body motion of individual grains, Computational Materials Science, 186 (2021) 109963.

[60] F. Abdeljawad, D.S. Bolintineanu, A. Cook, H. Brown-Shaklee, C. DiAntonio, D. Kammler, A. Roach, Sintering processes in direct ink write additive manufacturing: A mesoscopic modeling approach, Acta Materialia, 169 (2019) 60-75.
[61] Y. Yang, O. Ragnvaldsen, Y. Bai, M. Yi, B.-X. Xu, 3D non-isothermal phase-field simulation of microstructure evolution during selective laser sintering, npj Computational Materials, 5 (2019) 1-12.
[62] V. Kumar, Z. Fang, P. Fife, Phase field simulations of grain growth during sintering of two unequal-sized particles, Materials Science and Engineering: A, 528 (2010) 254-259.
[63] I. Greenquist, M. Tonks, M. Cooper, D. Andersson, Y. Zhang, Grand potential sintering simulations of doped UO2 accident-tolerant fuel concepts, Journal of Nuclear Materials, 532 (2020) 152052.
[64] K. Shinagawa, S. Maki, K. Yokota, Phase-field simulation of platelike grain growth during sintering of alumina, Journal of the European Ceramic Society, 34 (2014) 3027-3036.
[65] I. Greenquist, M.R. Tonks, L.K. Aagesen, Y. Zhang, Development of a microstructural grand potential-based sintering model, Computational Materials Science, 172 (2020) 109288.
[66] J. Deng, A phase field model of sintering with direction-dependent diffusion, Materials transactions, 53 (2012) 385-389.
[67] K. Ahmed, J. Pakarinen, T. Allen, A. El-Azab, Phase field simulation of grain growth in porous uranium dioxide, Journal of nuclear materials, 446 (2014) 90-99.
[68] Q. Yang, A. Kirshtein, Y. Ji, C. Liu, J. Shen, L.Q. Chen, A thermodynamically consistent phase-field model for viscous sintering, Journal of the American Ceramic Society, 102 (2019) 674-685.
[69] T. Shulin, Z. Xiaomin, Z. Zhipeng, W. Zhouzhi, Driving force evolution in solid-state sintering with coupling multiphysical fields, Ceramics International, 46 (2020) 11584-11592.
[70] Z. Zhao, X. Zhang, H. Zhang, H. Tang, Y. Liang, Numerical investigation into pressure-assisted sintering using fully coupled mechano-diffusional phase-field model, International Journal of Solids and Structures, 234 (2022) 111253.
[71] M. Seiz, H. Hierl, B. Nestler, An improved grand-potential phase-field model of solid-state sintering for many particles, Modelling and Simulation in Materials Science and Engineering, 31 (2023) 055006.
[72] A. Kirshtein, J. Brannick, C. Liu, Analysis of the energy dissipation laws in multi-component phase field models, Communications in Mathematical Sciences, 18 (2020) 875-885.
[73] F. Boyer, C. Lapuerta, Study of a three component Cahn-Hilliard flow model, ESAIM: Mathematical Modelling and Numerical Analysis, 40 (2006) 653-687.
[74] B.J. Kellett, F.F. Lange, Thermodynamics of densification: I, sintering of simple particle arrays, equilibrium configurations, pore stability, and shrinkage, Journal of the American Ceramic Society, 72 (1989) 725-734.
[75] H. Atkinson, Overview no. 65: Theories of normal grain growth in pure single phase systems, Acta Metallurgica, 36 (1988) 469-491.
[76] D. Weaire, N. Rivier, Soap, cells and statistics—random patterns in two dimensions, Contemporary Physics, 25 (1984) 59-99.
[77] L.-Q. Chen, Phase-field models for microstructure evolution, Annual review of materials research, 32 (2002) 113-140.
[78] P.C. Millett, M.R. Tonks, S. Biner, L. Zhang, K. Chockalingam, Y. Zhang, Phase-field simulation of intergranular bubble growth and percolation in bicrystals, Journal of Nuclear Materials, 425 (2012) 130-135.

[79] N. Moelans, B. Blanpain, P. Wollants, Quantitative analysis of grain boundary properties in a generalized phase field model for grain growth in anisotropic systems, Physical Review B, 78 (2008) 024113.
[80] M.-H. Giga, A. Kirshtein, C. Liu, Variational modeling and complex fluids, Handbook of mathematical analysis in mechanics of viscous fluids, (2017) 1-41.
[81] R. Chaim, G. Chevallier, A. Weibel, C. Estournès, Grain growth during spark plasma and flash sintering of ceramic nanoparticles: a review, Journal of Materials Science, 53 (2018) 3087-3105.
[82] N. Moelans, A quantitative and thermodynamically consistent phase-field interpolation function for multi-phase systems, Acta Materialia, 59 (2011) 1077-1086.
[83] L.K. Aagesen, Y. Gao, D. Schwen, K. Ahmed, Grand-potential-based phase-field model for multiple phases, grains, and chemical components, Physical Review E, 98 (2018) 023309.
[84] B. Nestler, H. Garcke, B. Stinner, Multicomponent alloy solidification: phase-field modeling and simulations, Physical Review E, 71 (2005) 041609.
[85] J. Hötzer, O. Tschukin, M.B. Said, M. Berghoff, M. Jainta, G. Barthelemy, N. Smorchkov, D. Schneider, M. Selzer, B. Nestler, Calibration of a multi-phase field model with quantitative angle measurement, Journal of materials science, 51 (2016) 1788-1797.
[86] M. Asoro, P. Ferreira, D. Kovar, In situ transmission electron microscopy and scanning transmission electron microscopy studies of sintering of Ag and Pt nanoparticles, Acta materialia, 81 (2014) 173-183.
[87] D. McLean, A. Maradudin, Grain boundaries in metals, Physics Today, 11 (1958) 35.
[88] M.C. Inman, H.R. Tipler, INTERFACIAL ENERGY AND COMPOSITION IN METALS AND ALLOYS, Metallurgical Reviews, 8 (1963) 105-166.
[89] G.E. Rhead, Surface self-diffusion and faceting on silver, Acta Metallurgica, 11 (1963) 1035-1042.
[90] S. Rothman, N. Peterson, J. Robinson, Isotope Effect for Self-Diffusion in Single Crystals of Silver, physica status solidi (b), 39 (1970) 635-645.
[91] R. Pareja, Migration Kinetics of (001) Twist Grain Boundaries in Silver Bicrystalline Films, International Journal of Materials Research, 72 (1981) 198-202.

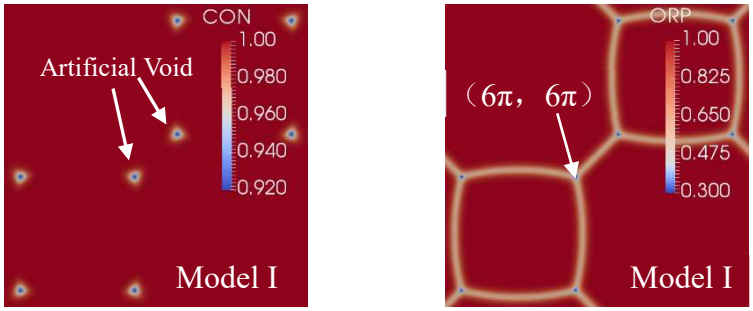

(a)

(b)

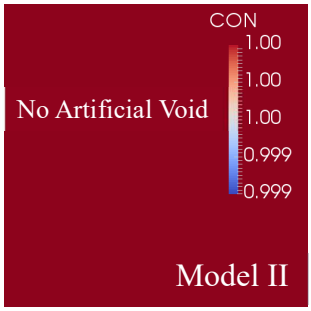

(c)

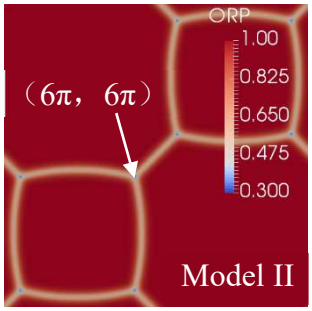

(d)

In fully dense power compact under sintering, existing Model I may produce artificial voids and the proposed Model II avoids this issue. Artificial voids may delay microstructure evolution. The figure shows microstructure morphologies when a triple junction reaches the selected spatial point (6π，6π) after the quadruple junction splits into triple junctions from the respective Model I (a-b) when t = 15s and Model II (c-d) when t = 14.1s.